Dynamic Focusing of Large Arrays for Wireless Power Transfer and Beyond

Ali Hajimiri⬛, *Fellow, IEEE*, Behrooz Abiri, *Member, IEEE*, Florian Bohn⬛, *Member, IEEE*,
Matan Gal-Katziri⬛, *Member, IEEE*, and Mohith H. Manohara⬛, *Student Member, IEEE*

Abstract—**We present architectures, circuits, and algorithms for dynamic 3-D lensing and focusing of electromagnetic power in radiative near- and far-field regions by arrays that can be arbitrary and nonuniform. They can benefit applications such as wireless power transfer at a distance (WPT-AD), volumetric sensing and imaging, high-throughput communications, and optical phased arrays. Theoretical limits on system performance are calculated. An adaptive algorithm focuses the power at the receiver(s) without prior knowledge of its location(s). It uses orthogonal bases to change the phases of multiple elements simultaneously to enhance the dynamic range. One class of such 2-D orthogonal and pseudo-orthogonal masks is constructed using the Hadamard and pseudo-Hadamard matrices. Generation and recovery units (GU and RU) work collaboratively to focus energy quickly and reliably with no need for factory calibration. Orthogonality enables batch processing in high-latency and low-rate communication settings. Secondary vector-based calculations allow instantaneous refocusing at different locations using element-wise calculations. An emulator enables further evaluation of the system. We demonstrate modular WPT-AD GUs of up to 400 elements utilizing arrays of 65-nm CMOS ICs to focus power on RUs that convert the RF power to dc. Each RFIC synthesizes 16 independently phase-controlled RF outputs around 10 GHz from a common single low-frequency reference. Detailed measurements demonstrate the feasibility and effectiveness of RF lensing techniques presented in this article. More than 2 W of dc power can be recovered through a wireless transfer at distances greater than 1 m. The system can dynamically project power at various angles and at distances greater than 10 m. These developments are another step toward unified wireless power, sensing, and communication solutions in the future.**

Index Terms—**Calibration, dynamic refocusing, orthogonal basis, phased array, power focusing, pseudo-Hadamard matrices, pseudo-orthogonal bases, RF lensing, wireless power transfer at a distance (WPT-AD), wireless power transfer.**

I. INTRODUCTION

PHASED arrays have found numerous applications since their invention by Braun [1] in 1905. The vast majority of their applications and a large fraction of the analytical and experimental techniques have been concentrated on the radiative far-field (Fraunhofer) region. Many works have been published on classical far-field (infinity) beam-forming and scanning procedures for phased arrays [2]–[6]. A large number of emerging applications, however, are intended to operate in the radiative near-field (Fresnel) region and impose unique challenges. Radiative wireless power transfer at a distance (WPT-AD), volumetric sensing and imaging, high-efficiency high-throughput communication, very-large-scale arrays, and optical phased arrays (OPA) can benefit from the ability to form a focal point in 3-D, also known as free-space dynamic lensing [7] or simply *RF lensing*, hereafter.

The dynamic lensing process, in its most general form, is done in a highly interactive environment with moving objects, indoor reflections, mechanical vibrations, and even physical contact with the radiator itself. Most of the previously published works characterize the far-field behavior dependence on each element's phase and amplitude setting. This is done either as a factory setting or *in situ* [8], [9], using proximal field receivers at the array [10], element [11] level, or inter-element measurements [12], [13], and requires some assumptions about the elements' radiation patterns [14], [15] and the array's deployment environment. Essentially, any unaccounted for dynamic interference translates to an error.

This calls for the development of new approaches and procedures to synthesize EM fields in highly interactive, strongly multi-path, and constantly changing environments (e.g., inside an occupied home) with arrays that can themselves be mechanically flexible [16], [17], non-planar [15], [18], nonuniform [19], non-Cartesian [20], or physically shape-shifting [21]. Such settings are substantially different from the idealized far-field free space models of classical phased arrays. This article presents methods and architectures conducive to such systems. While the primary emphasis of this article is on wireless power transfer, the algorithms and techniques discussed here are also applicable more broadly to RF and optical arrays, efficient communications, and 3-D sensing and ranging.

On the wireless power transfer front, a future where WPT-AD sources are ubiquitous could change the nature and utilization of electronic devices that need energy for operation, perhaps in a similar way to that in which ubiquitous Wi-Fi changed the connectivity and storage models from local to distributed. For instance, continuous wireless powering of portable personal devices, such as smartphones, can significantly enhance their utility. In the long run, it will reduce the demand for the amount of energy that needs to be carried by such devices, potentially leading to lighter, smaller devices due to smaller battery size. Also, smaller devices ranging

Ali Hajimiri, Matan Gal-Katziri, and Mohith H. Manohara are with the Department of Electrical Engineering, California Institute of Technology, Pasadena, CA 91125 USA (e-mail: hajimiri@caltech.edu).

Behrooz Abiri and Florian Bohn were with the Department of Electrical Engineering, California Institute of Technology, Pasadena, CA 91125 USA. They are now with GuRu Wirelesss Inc., Pasadena, CA 91103 USA.

from wireless mice and keyboards to thermostats, security sensors, cameras, and other Internet-of-Things (IoT) devices can benefit from WPT-AD, as it eliminates the need to plug them in or change the battery. In the mid-range, various devices such as drones and robots could also be powered wirelessly. On the other end of the spectrum, long-range power transfer on earth and from space may present intriguing alternatives to power distribution networks in the long run [22].

Radiative microwave WPT-AD using parabolic transmitting antennas has been envisioned [22] and demonstrated [23] long ago. However, it has been only recently that practical commercial implementation of such a system with reasonable cost and size and the ability to dynamically track and focus power on potentially moving client devices at arbitrary and unknown locations can be considered. This is primarily due to the emergence of practical silicon mm-wave integrated circuits [24]–[32] with their almost magical complexity-to-cost-and-size ratio.

Radiative WPT-AD lensing arrays operate in both radiative near- and far-field regions, where their objective is to rapidly and efficiently form focal point(s) of power at finite distances to maximize the recovered energy. The maximum energy transfer (essentially by definition)[1] happens in the radiative near-field (Fresnel), which can extend to long absolute distances for smaller wavelengths.[2] This leads to the dynamic RF lensing approaches that are more general than the conventional far-field beamforming and beamsteering that simply correspond to focusing at infinity. Although wireless power transfer of a little over 1 mW at distances less than 5 cm has been demonstrated [33], to the best of our knowledge up until now, there has been no published demonstration of a silicon-array-based WPT-AD system that can recover several watts of dc power at distances over a meter with the ability to dynamically move the focal point.

In the rest of this article, we will discuss the theory, architecture, circuits, algorithm, and performance of such WPT-AD systems while introducing concepts and methods more generally applicable to arbitrary and nonuniform arrays beyond WPT-AD. We start with a discussion of RF lensing and associated electromagnetics (EMs), and fundamental limits and bounds (see Section II) followed by an overview of the challenges for focusing in large arrays (see Section III). Next, we present the details of a generalized adaptive algorithm based on orthogonal and pseudo-orthogonal

bases (see Section IV) and rapid dynamic refocusing (see Section V). We will present the IC and system hardware architecture and implementation details in Section VI. Next, we review an emulator and its results (see Section VII) and then physical measurements of the system (see Section VIII). The generation of the orthogonal and pseudo-orthogonal bases is presented in the Appendix. This article provides the details of a silicon-based wireless power transfer system that can serve as a stepping stone toward future WPT-AD systems.

II. RF Lensing

RF lensing refers to a set of techniques to shape, manipulate, focus, and refocus the EM field, often analogous to how optical devices manipulate, shape, and focus visible light (which themselves are EM waves) [7]. The dynamic electronic control of the properties of the radiated field of elements within an array (e.g., phase and amplitude) enables such manipulation to happen adaptively akin to a real-time malleable optical system. RF lensing functionalities, some of which are discussed in this article, are at the heart of a truly universal WPT-AD system.

Focusing is one of the key RF lensing functions, where the RF energy is concentrated at the desired and dynamically programmable focal point(s) in the radiative near-field. This can be achieved by manipulating the phase (and possibly amplitude) of the elements of an array.[3] There exist parameter setting(s) for individual elements that, when operating in concert, produce the desired field distribution, be it a forming a focal point, maximizing the total recovered dc power at an unknown location, or any other desirable field profile permissible by laws of physics.

Fig. 1 shows a simple example of focusing in free space, where a generator unit (GU) array creates a focal point of energy on a recovery (or receiving) unit (RU) array [7]. Although both GU and RU are shown as uniform, planar, rectangular multi-element arrays here, most of the techniques presented in this article are applicable in nonuniform, non-planar, mechanically flexible, and actively shape-shifting, with non-rectangular grids in highly scattering environments (e.g., indoors) [15]–[21]. This is one of the primary advantages of RF lensing techniques.

A. GU-to-RU Radiative Coupling Model

In general, a system consisting of a GU with G elements and an RU with R elements (such as the one shown in Fig. 1) can be viewed as a $(G+R)$-port network that can be characterized using a $(G+R) \times (G+R)$-element S-parameter matrix capturing coupling among all the elements

$$\mathbf{S} = \left[\begin{array}{c|c} [\mathbf{S}_{\text{GU}}]_{G \times G} & [\hat{\mathbf{S}}]_{G \times R} \\ \hline [\hat{\mathbf{S}}^{\dagger}]_{R \times G} & [\mathbf{S}_{\text{RU}}]_{R \times R} \end{array} \right] \tag{1}$$

which consists of $\hat{\mathbf{S}}$, which characterizes the radiative coupling between each GU radiator port and each RU antenna port, and matrices $\mathbf{S}_{\text{GU}}$ and $\mathbf{S}_{\text{RU}}$, which characterize the local coupling among the local ports of the GU and RU, respectively.

Determination of $\mathbf{S}$ using direct EM propagation simulation (e.g., using FDTD)[4] of every spatial configuration of a system

---

[1]Radiative far-field (Fraunhofer) is defined as the distances beyond which the phase variations of the wavefront across the receiver aperture do not exceed some predetermined amount (e.g., $\pi/8$ or $1°$) [4]. To be in the radiative far-field, the receiver aperture must cover a small fraction of the illuminated main lobe (representing a small numerical aperture). When this condition is held, the received power drops as inverse square law. For a generator (transmitter) and receiver facing each other with non-incremental circular apertures of diameters, d_g and d_r, the $\pi/8$-boundary distance of the radiative near-field (Fresnel) and far-field is calculated to be $R_{\pi/8} \approx 2\, d_g d_r / \lambda$, where λ is the wavelength of interest. The distance for $1°$ phase variation across the receive aperture is much larger, around $R_{1°} \approx 50\, d_g d_r / \lambda$. From (10) (derived later), these correspond to the estimated power transfer efficiencies of 30% and 1% for the $\pi/8$- and $1°$-variation distances, respectively.

[2]For example, an orbital wireless power transfer station and a ground recovery station with diameters of 3 km and 1 km operating at 10 GHz have a $\pi/8$-boundary of $200\,000$ km, way in excess of the geosynchronous orbit of $R_{GEO} = 36\,000$ km. On the other end of the spectrum, a pair of 30 cm and 10 cm generation and recovery units operating at 24 GHz have a $\pi/8$-boundary of more than 6 m.

[3]In addition, the directivity, pattern, impedance, or other characteristics of the element may be controllable.

[4]Finite difference time domain.

Fig. 1. 8×8-GU ($G = 64$) facing a 2×2-RU ($R = 4$) at a $45°$ angle with conceptual field profile under focusing.

Fig. 2. Patch antenna as an antenna array element with spacings of d_x and d_y in the x- and y-directions.

with a large number of elements on the transmitter and receiver is not computationally scalable. It can become prohibitive when multiple configurations with varying orientations are to be considered with a large number of elements on both GU and RU sides, and the GU-RU spacing is several orders of magnitude larger than the fine (yet important) features of the individual radiators. To deal with this situation, we use an alternative approach that can rapidly determine and recalculate the complex energy coupling coefficient between each of the radiators of the GU and each of the elements on the RU.

An important observation is that, in most scenarios,[5] while GU and RU arrays are in each other's radiative near-field, at the individual element level, the coupling can be well-approximated using the elements' far-field patterns within the array. In its simplest form, the approach uses a single EM simulation to determine the far-field radiation pattern of one GU element within a large array.[6] A similar simulation is done for an RU element (also within an array) to determine its far-field pattern. These results are then used to estimate the coupling between each of the G elements of the GU and R elements of the RU to produce a $G \times R$-matrix of complex coupling coefficients.[7] This is done by converting the local coordinates (position and orientation) of the single elements in question within the GU and the RU to a global coordinate system that is used to calculate the coupling using the far-field patterns of the individual GU and RU elements at their relative spacing and orientation with respect to each other.

This approach allows for modeling of any arbitrary spatial arrangement and orientations of the GU and RU. At the element level, it uses a one-time electromagnetically simulated radiation pattern of each element (or groups of elements) in an array (or the exact simulated multi-port antenna array pattern of a group of antennas) to determine $\hat{\mathbf{S}}$. It is important to use the element pattern in the array in the above simulations, as it can be quite different from the standalone element, as will be discussed next.

B. Gain and Directivity Limits for Antennas Within an Array

In an infinite 2-D array (a surrogate for a large array), there is a fundamental upper bound on the directivity (and

thus gain) of each element, independent of the pattern of the standalone radiating element (evaluated when other elements are not present). Consider the uniform planar thin 2-D antenna array of Fig. 2 with element pitch of d_x and d_y along the x- and y-axes, respectively. Assuming an incident plane wave impinging perpendicular to the array, each d_x-by-d_y rectangle presents an available collection area of

$$A_{\text{av}} = d_x d_y. \tag{2}$$

Assuming perfect aperture coupling, meaning that all the incident power is recovered and coupled into the antenna port without any loss, the element's maximum effective aperture, A_e, will be that same as A_{av}. For a single-mode single-port antenna, the directivity is related to the effective aperture through

$$D = 4\pi \frac{A_e}{\lambda^2}. \tag{3}$$

Thus, the maximum directivity (and, thus, maximum gain that is always less than directivity) of a single element within the array is fundamentally limited to

$$D_e \leq 4\pi \frac{d_x d_y}{\lambda^2}. \tag{4}$$

For example, for an array with $d_x = d_y = \lambda/2$, the element directivity (and gain) cannot exceed π, i.e.,

$$D_{e,\lambda/2} \leq \pi. \tag{5}$$

It should be noted that (4) and (5) are per element upper bounds applicable only for elements within a large uniform array.

An important corollary is that no matter the standalone gain of the element, once placed in a large[8] array, it cannot exceed the limit of (4). For instance, making a large $\lambda/2$-array of 20-dB helical antennas is not particularly effective as the element gain will not exceed π. Thus, one should not blindly multiply the standalone element gain by the array gain to predict the array's radiative far-field behavior. This reduction in gain occurs through the near-field coupling of neighboring antennas and is a *manifestation of conservation of energy*, and it is applicable to any kind of antenna element in an infinite array. Fig. 3 compares the simulated antenna gain of a single standalone patch element of Fig. 2 with the exact same elements in the middle of a large $\lambda/2$-array. It is clearly seen that, while the standalone element gain exceeds that of

---

[5]This may also apply to other scenarios involving large arrays at finite distances for non-WPT-AD applications.

[6]This ignores the effect of edge elements.

[7]Alternatively, we can use complete G-port radiative far-field simulations of the GU and/or RU. These results can then be used for element-wise calculations used to obtain $\hat{\mathbf{S}}$.
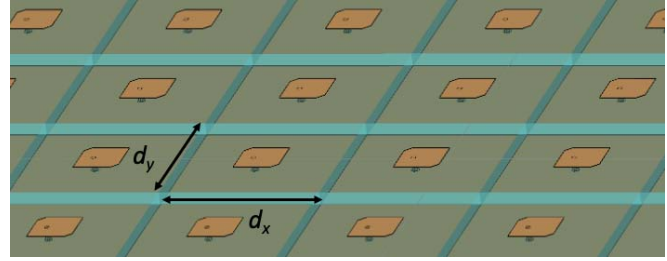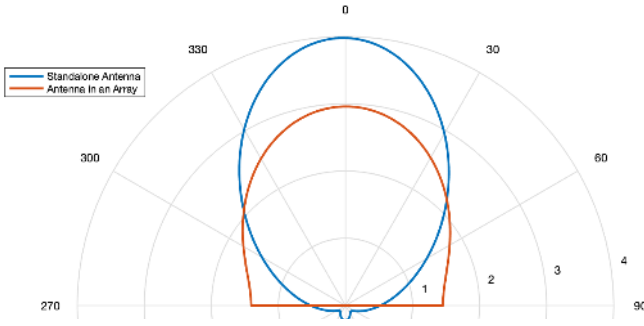
[8]Infinite to be exact.

Fig. 3. Gain reduction of the patch antenna elements of Fig. 2 within the array compared with standalone gain. The infinite array results are obtained by using periodic boundary conditions in the x- and y-directions. The results are in absolute and not in dB.

(5), it drops below π when that very same element is placed within a large $\lambda/2$-array of similar elements. The shape of the radiation pattern changes in addition to its peak value. This is why it is important to use the radiative pattern of the element in an array for the simulation and emulation of the GU and RU to avoid (potentially gross) errors.

C. Optimum

For a known $\hat{\mathbf{S}}$ and arbitrary (yet known) set of amplitudes and phases of all the GU elements shown by G-element vector $\mathbf{a}$ with complex elements $a_g e^{j\phi_g}$, the power transfer efficiency is given by

$$\eta = \frac{\mathbf{a}^\dagger \hat{\mathbf{S}}^\dagger \hat{\mathbf{S}} \mathbf{a}}{\mathbf{a}^\dagger \mathbf{a}}. \tag{6}$$

Finding the phases (and amplitudes) that maximize this is a standard mathematical optimization problem that can be solved in a computationally efficient way using a number of optimization methods. For instance, the special case of uniform amplitude drive reduces to

$$\eta_{\text{opt}} = \frac{1}{G} \max_{\Phi} |e^{-j\Phi} \hat{\mathbf{S}}^\dagger \hat{\mathbf{S}} e^{j\Phi}|. \tag{7}$$

The objective of the WPT-AD system (and its associated algorithm) is to get as close as possible to this value without prior knowledge of $\hat{\mathbf{S}}$, which can constantly change in a real system.

D. Estimate

An estimate for power transfer efficiency can be obtained by assuming a large array where the individual element gain is limited by (4) and the edge element effects[9] can be ignored. Assuming a square grid ($d_x = d_y$) for both the GU and the RU, the far-field power transfer between element g of the GU and element r of the RU can be approximated as

$$|s_{gr}|^2 = \frac{A_{e,g}(\theta_g, \varphi_g) A_{e,r}(\theta_r, \varphi_r)}{R_{gr}^2 \lambda^2} \approx \frac{d_g^2 d_r^2}{R_{gr}^2 \lambda^2} \tag{8}$$

[9]Examples of edge effects are increased effective aperture on the open side of the edge elements or endfire radiation of a finite array.

where $A_{e,g}(\theta_g, \varphi_g)$ and $A_{e,r}(\theta_r, \varphi_r)$ are the visible apertures of the elements in the respective angles θ and φ with respect to the GU and RU normal planes, d_g and d_r are the GU and RU element spacings, R_{gr} is the straight-line free-space distance between those elements, and λ is the wavelength. The second equation assumes broad-side-to-broad-side coupling of GU and RU. Assuming an equal power transmission of p_g from each GU element, the power received by the rth RU element will be maximized when all components add in phase (coherently) and are given by

$$p_r \approx \left(\sum_{g=1}^{G} |s_{gr}| \right)^2 p_g \approx \frac{d_g^2 d_r^2}{R_{Gr}^2 \lambda^2} G^2 p_g = \frac{d_g^2 d_r^2}{R_{Gr}^2 \lambda^2} G P_{\text{GU}} \tag{9}$$

where, in the last step, $P_{\text{GU}} = G p_g$ is the total GU transmitted power.[10] Assuming that different RU elements' powers can be combined and maximized simultaneously[11] and under the optimum setting, the combined power of all R elements of RU can be approximated as $P_{\text{RU}} \approx R \cdot p_r$, yielding the transfer efficiency of

$$\eta = \frac{P_{\text{RU}}}{P_{\text{GU}}} \approx \frac{R \cdot p_r}{P_{\text{GU}}} \approx \frac{A_G A_R}{R_{GR}^2 \lambda^2} \tag{10}$$

where $A_G = G d_g^2$ and $A_R = R d_r^2$ are the total areas of the GU and RU, respectively. This expression provides an estimate of the transfer efficiency for arrays with aspect ratios (length-to-width) of close to 1. It can also be multiplied by the GU and RU element-in-the-array patterns to account for off-broadside interactions. It is noteworthy that, for very large A_G and/or A_R, or small R, this estimate can produce obviously nonphysical results by becoming greater than 1 and so would be physically capped at unity.[12]

E. Upper and Lower Bounds

An upper bound on the maximum power transfer from the GU to the RU can be obtained by adding the maximum powers that each RU element can receive if the phase (and amplitude) setting of the GU is selected to individually maximize the power at that element with no consideration of other RU elements. Since it may not be possible to sustain these potentially different settings for different RUs simultaneously, this establishes an upper bound expressed as

$$\eta \leq \frac{\sum_{r=1}^{R} \left(\sum_{g=1}^{G} |a_g \hat{s}_{gr}| \right)^2}{\sum_{g=1}^{G} |a_g|^2} \tag{12}$$

[10]It approximates the distance and angle to each element with an average distance and angle from the center of the GU to the center of RU.

[11]This assumption may or may not be accurate depending on the actual orientations, dimensions, and distance of the RU and GU. For very small distance, certain oblique angles, and so on, this cannot be achieved due to the interference pattern on the RU surface. The most accurate estimate can always be obtained using (7).

[12]An empirical expression that smoothly caps the max to unity is

$$\eta \approx 1 - e^{-\frac{A_G A_R \cos(\theta_g) \cos(\theta_r)}{R^2 \lambda^2}} \tag{11}$$

which, for uniform GU amplitude drive, simplifies to

$$\eta \le \frac{1}{G} \sum_{r=1}^{R} \left(\sum_{g=1}^{G} |\hat{s}_{gr}| \right)^2 . \tag{13}$$

A physically realizable lower bound for the optimum phase setting in GU can be found.[13] Note that, for a given phase of an element in the GU, in general, different phases may be received at each RU element. If these outputs were to be simply added in the complex domain (combining before individual rectification), a $G \times 1$-vector, $\bar{\mathbf{S}}_{[G \times 1]}$ would capture the coupling from individual GU ports to the RU unified output

$$\bar{s}_g = \sum_{r=1}^{R} \hat{s}_{gr}$$

which leads to the lower bound

$$\eta \ge \frac{1}{G} \sum_{r=1}^{R} \sum_{g=1}^{G} \frac{\bar{s}_g^*}{|\bar{s}_g|} \cdot \hat{s}_{gr} \tag{14}$$

where the first fraction is simply the optimum phase for each GU element (conjugate phase of element g).[14]

F. Choice of Frequency

The choice of frequency plays a major role in the range, size, transfer efficiency, economy, and practicality of a WPT-AD system and is perhaps the most significant parameter of choice. This is evident from the presence of wavelength squared in the denominator of (10). Simply put, everything else being equal, a doubling of operation frequency can translate to a factor of 4 reductions in the size of the GU or RU (or a combination thereof) at a given efficiency, doubling of range for a given GU and RU size, or a fourfold increase in transfer efficiency subject to the cap discussed in Section II-D and footnote 11. A plot of the best-estimated transfer efficiency of the system from (11) at four different frequencies (see Fig. 4) shows this dependence and the strong preference for a higher frequency of operation.

III. FOCUSING CHALLENGE IN LARGE ARRAYS

A practical radiative WPT-AD system utilizes one or more GUs to dynamically focus EM energy on various RUs, which converts the focused EM beam's energy to usable dc power using a chain of antennas, rectifiers, and regulators. The GU uses multiple synchronized RF sources and antennas to maximize the power recovered by the RU(s) at their potentially unknown locations in 3-D space. This focusing is achieved through constructive interference by adjusting the

---

[13]It is obvious that the random phase setting lower bound is simply 0.

[14]The second lower bound can be obtained by calculating the optimum conjugate phase setting in GU for each RU element, repeating this process for every RU element, and using the GU setting that led to the highest individual RU element power, to find the total RU output power to find another physically achievable lower bound

$$\eta \ge \max_r \left| \sum_{g=1}^{G} \hat{s}_{gr}^* \hat{s}_{gr} \right| . \tag{15}$$
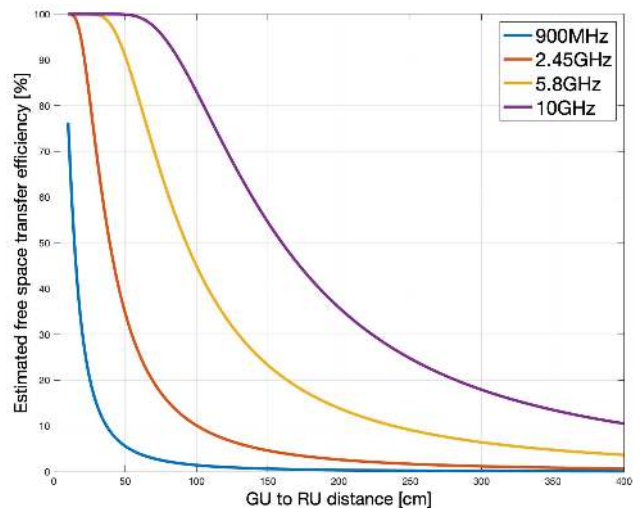

Fig. 4. Approximate maximum transfer efficiency plot for a 0.4×0.4 m² GU and a 0.1×0.1 m² RU versus distance using (11).
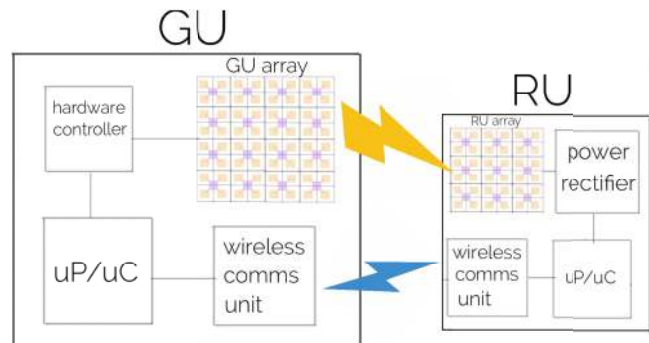

Fig. 5. High-level architecture of a GU wirelessly transferring power to an RU.

phase (and amplitude) of each source and rapidly switching the beam location to distribute the power among different locations in different proportions using a time-division multiplexing (TDM) scheme. The RUs can communicate with the GU and provide information using either an active or a passive radio channel. Fig. 5 shows an example of the high-level architecture of such a system with one GU and one RU.

In many WPT-AD scenarios, the location of the RU is not known ahead of time, can frequently, and continuously changes, necessitating a rapid focusing algorithm that can be refocused over a short duration of time. Furthermore, as will be seen in Section VI, the absolute phase values of the individual elements may be effectively random. Also, in many practical scenarios, there are various bandwidth and latency limitations on the communication between GU and RU. In addition, in highly scattering environments (e.g., indoors), the optimum phase setting may be significantly different from the free-space ones due to reflections and obstructions. Thus, the system should be able to focus and refocus rapidly without any advance knowledge about the absolute phase of each element and have the ability to pipeline and batch process multiple settings with minimum power spillover (power not recovered by an RU).

For a given relative location and orientation of an RU with respect to a GU, there exists a combination of phases of the RF power sources on the GU that maximizes the recovered energy for a given RU shape, location, and orientation.[15] However, finding such combinations rapidly and reliably (i.e., focusing on a given location and orientation) can be challenging in a large array. To illustrate this, consider a transmitter array with G elements, where the phase of each element can be changed by P phase steps. The number of possible phase combinations in such a system is P^G, which grows exponentially with the number of elements. For example, in a small array with 100 elements, where the phase of each element is determined by an 8-bit word, the number of possible phase combinations is given by[16] $256^{100} = 2^{800} \approx 10^{240}$. This makes a brute-force search through all possible combinations impossible.[17] This situation is further exacerbated for larger arrays.[18]

It is obvious that, other approaches can be used to mitigate this situation. In theory, sweeping through the phase setting of each element individually, while the other elements are maintained at a constant phase, can change the exponential growth to a linear one by sweeping through $P \cdot G$ phase settings, which scales much more favorably with the array size.[19] In this approach, a batch of phase settings are programed into the array in fast succession; the power received by the RU array is monitored; and the index of the phase setting with the highest received power at the RU is transmitted back to the GU either after each sweep or a predetermined number of sweeps. The number of distinct phase settings tested within each batch that is reported all at once within each communication interval is called communication run length (CRL). Upon receipt of these indexes, the GU will adjust the phases of those elements to the value(s) producing the largest recovered power and continues the sweep of remaining elements.[20]

A variant of this approach is the classical gradient descent algorithm [34], which, in the absence of noise and certain other non-idealities, is mathematically proven to arrive at the global optimum, as long as the optimization objective function is convex [35]. Such approaches may settle at the local optimum in the case of non-convex function. Fig. 6 visualizes the variations of the received power at some small point in space with three radiative sources with the same amplitude when the phases of two of them (ϕ_1 and ϕ_2) are varied between 0 and $360°$ (2π), while the third source's phase is held constant (ϕ_0). It can be seen that, in the absence of noise and other non-idealities, a gradient descent (ascent in this case) to the peak can end up at any of the four local optima (maxima in this case), designated as P_1 to P_4. As a result, in this particular maximization of power using the method of element phase
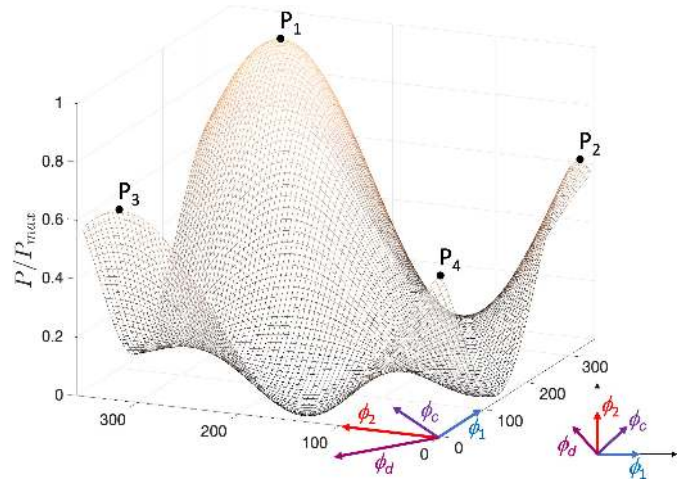

Fig. 6. Visualization of the focusing space of a three-element array versus ϕ_1 and ϕ_2, when the third element also radiates with the same amplitude and constant reference phase.

variation, the objective function is not necessarily convex within the range of $[0, 2\pi)$ for an arbitrary initial phase.

However, the search space periodically repeats with a period of 2π for all element phases, and hence, any gradient-based approach will reach the maximum power if the phase is allowed to progress beyond the boundaries of the $[0, 2\pi)^G$ sized box[21] of phase variables, as then the algorithm will arrive at a phase setting that results in maximum transferred power. For example, in Fig. 6, any movement toward points P_2, P_3, or P_4 will eventually end up at P_1 through the modulo-2π wrapping. This makes the modulo-modified function effectively convex.[22] Thus, in the absence of noise and other non-idealities, gradient descent type algorithms are mathematically guaranteed to arrive at the global optimum. While this approach theoretically solves the problem, as is often the case, the situation in practice is quite different.

Such independent phase optimization approaches often result in small variations in the received power at the RU, particularly when a large array is involved, since the power fluctuations as the phase is swept are due to interference between one element and the rest of the elements. In practice, there are additive non-idealities, such as amplitude and phase noise in the GU, amplitude, and quantization noise in the RU, and RF interference, as well as nonlinear effects, such as oscillator and PLL pulling and coupling in the GU and nonlinear mixing in the RU. These non-idealities lead to large errors in the detected signal, which can result in a significant reduction in the dynamic range and accuracy of the RU evaluations and, thus, the quality of focusing. Furthermore, as the fine-tuning of the phase increases toward the end of the focusing process, the progressively smaller variations get almost entirely buried by the aggregate noise and interference from other elements. This results in inferior focusing, especially for fine phase adjustments, which translates to significantly lower recovered

---

[15]Power amplifiers often perform best near their peak power, so, for this discussion, we focus on the phase changes.

[16]Using $2^{10} \approx 10^3$.

[17]Even trying one billion combinations per second, it will take 3×10^{223} years, or 3×10^{213} times the life of the universe to complete the search!

[18]Or when amplitude control is used in addition to changing the phases of the individual elements to further minimize power spillover.

[19]A very manageable $100 \times 256 \approx 2.6 \times 10^4$ states in our example.

[20]An often-predefined mathematical function describing the amplitude settings for the GU, known as an apodization or windowing function, can also be applied to produce and refine a particular desirable pattern shape.

[21]More accurately, a G-dimensional hyper-cube.

[22]Perhaps, it should be called "cyclically convex" because of its periodicity with multiple equivalent maxima, any of which is the global maximum.
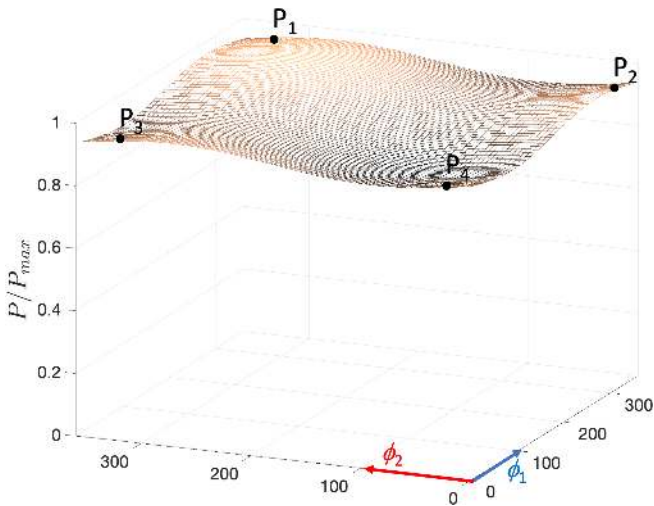
Fig. 7. Visualization of the focusing space of a 64-element array versus ϕ_1 and ϕ_2, when all remaining 62 elements radiate at phases that result in complete constructive interference at point of interest.
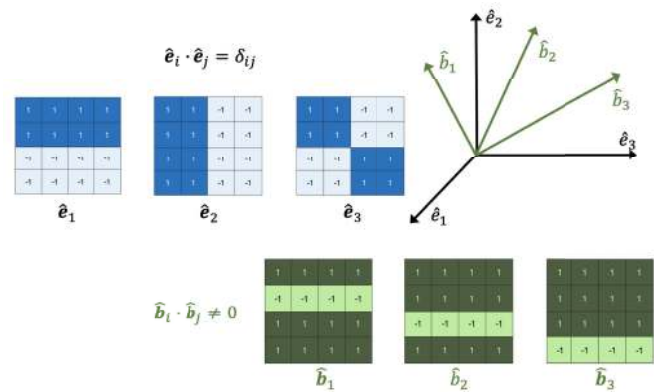

Fig. 8. Linearly independent, but non-orthogonal partial (three out of 16) mask-set ($\mathbf{b}_1$, $\mathbf{b}_2$, and $\mathbf{b}_3$) and orthogonal partial (three out of 16) mask-set ($\mathbf{e}_1$, $\mathbf{e}_2$, and $\mathbf{e}_3$).

power at the RU than the GU power capacity. This can be seen in the conceptual plot of power variations with respect to the phase variations of two elements in a larger array (64 elements in this case), as shown in Fig. 7. Compared with Fig. 6, it is clear that single-element variations produce smaller fractional changes in larger arrays. In the presence of amplitude and phase noise, this can render them ineffective as the number of array elements grows.[23]

IV. MULTI-ELEMENT FOCUSING USING 2-D (PSEUDO-)ORTHOGONAL BASES

The phase and amplitude settings of an $M \times N$-element ($G = MN$) transmitter array in a power generation unit (GU) present a complex $M \cdot N$-dimensional basis for the vector space of all the GU settings, where the phase and amplitude of the radiator at index (m, n) can be viewed as elements of an M-by-N matrix. If a constant amplitude is assumed and only phases are varied, the vector space can be represented as a real vector space with actual values of the individual phases as the elements of a matrix.[24] Such a vector space can be spanned using many different sets of basis matrices. In such a space, the inner product of two matrices $\mathbf{a}$ and $\mathbf{b}$ is defined as[25]

$$\langle \mathbf{a}, \mathbf{b} \rangle = \langle \mathbf{b}, \mathbf{a} \rangle = \sum_{i=1}^{M} \sum_{j=1}^{N} a_{ij} b_{ij}. \qquad (16)$$

A complete basis for this space would consist of G matrices ($G = MN$), as it is a G-dimensional vector space. We refer to the matrices that form the basis for the space as masks. The

simplest examples of such masks are the ones consisting of all-zero matrices with only one element being one, where, for each matrix, the single one appears in a different location. Another simple, yet relevant, example is shown in Fig. 8, where the three independent basis matrices (masks) (with elements being -1 and 1), $\mathbf{b}_1$, $\mathbf{b}_2$, and $\mathbf{b}_3$, are linearly independent, yet not orthogonal, while masks $\mathbf{e}_1$, $\mathbf{e}_2$, and $\mathbf{e}_3$ are orthogonal (and, thus, obviously also linearly independent), in the 16-D space of the 4×4-matrices.

A complete mask-set (basis) that spans the entire vector space of parameters is often necessary, as an incomplete basis could result in suboptimal focusing and, thereby, reduced efficiency in the case of WPT-AD. This is because parts of the search space would remain unexplored. While many different mask-sets (basis functions) are possible, different basis functions could be preferred depending on the scenario.

An important observation is that a change of basis does not change the (cyclic-)convexity of the focusing objective function (e.g., Fig. 6), and thus, as long as a complete basis is used, the same mathematical guarantees for arriving at the global optimum[26] that existed for the individual phase adjustment approach would also apply for the G-dimensional space.[27]

The signal-to-noise ratio (SNR) plays a significant role in effective focusing. As the phase variations become smaller in later stages of the focusing process when there is a large distance between the GU and the RU, as one or both are obscured by conductive or absorbing materials or placed in undesirable orientations with respect to each other, the SNR can significantly degrade, lowering the quality of the focusing.

The SNR challenges can be alleviated by sweeping the phase (and possibly amplitude) of multiple elements in the array simultaneously using masks that vary the phase of a large number of elements simultaneously. This approach produces large signal variations due to the constructive and destructive interference of a larger number of elements. To see this,

---

[23]Independent-phase-adjustment algorithms assume that the optimum phase settings of different elements are independent of each other. In reality, non-idealities can produce undesirable projections and imperfections if the phases were individually and independently optimized.

[24]For a non-constant amplitude setting, the matrix elements can be complex phasors, $A_{mn}e^{j\phi_{mn}}$.

[25]It is noteworthy that $\langle \mathbf{a}, \mathbf{b} \rangle = \text{tr}(\mathbf{a}^T \mathbf{b})$.

[26]In the absence of noise and other non-idealities.

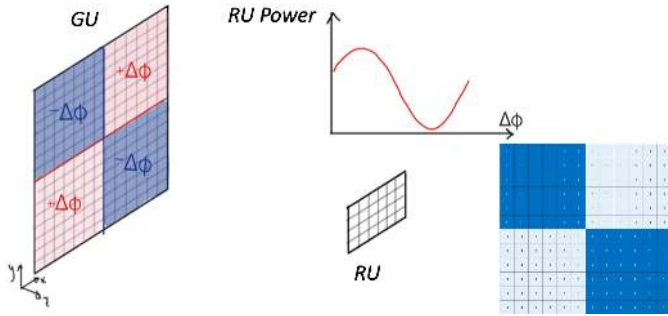[27]Assuming gradient-descent-type approaches.

Fig. 9. Received power variations at RU due to phase change of half of the GU elements with respect to the others in an example of the GU-RU pair with a 2-D signed mask.
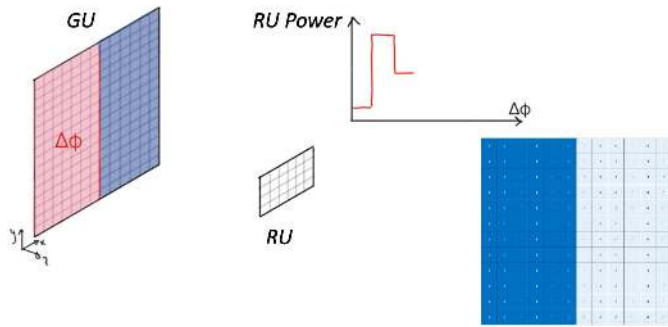

Fig. 10. Received power fluctuations at RU due to a small number (three in this example) of phase changes of half of the GU elements with respect to the others in an example of the GU RU pair with a 2-D binary basis vector different from the one in Fig. 9.

imagine an extreme scenario, where the focusing is already achieved, and the signal power is focused at a given 3-D focal point (see Fig. 9). If half of the array elements (the red group) are swept by $\Delta\phi$ and the other half (the blue group) swept by $-\Delta\phi$, the signal power can be changed across its entire usable dynamic range, from maximum power, P_{max}, to 0, as $\Delta\phi$ goes from 0 to 90°, as shown in Fig. 9. While sweeping the phase of a large number of elements simultaneously can provide significant improvements in the SNR at the RU, it may not be immediately clear how it can be used to identify the optimum setting for each element of a large array. Next, we present a framework using orthogonal mask sets for the dynamic focusing algorithm of an arbitrary array at an unknown location to address this question.

A. Orthogonal Mask-Phase Sweep

There are many different masks that can achieve the full power sweep of Fig. 9. The phase shift may be done differentially (with one group moving in the opposite direction of the other group) (masks with element +1 or −1, which we will call signed masks) or in a one-sided fashion, where only one group of phases is swept without the other group moving (with mask elements at 0 or 1, hereafter referred to as binary masks, as in the example of Fig. 10). Each mask would sweep the phases of different groups of elements, while the RU monitors and records the received power.

The phase of the elements within each mask can be swept over dynamically adjustable phase sweep ranges (PSRs) and with an arbitrary number of phase steps (NPS) within each overall iteration of the loop. (For example, PSR = 180° and NPS = 4 correspond to $\Delta\phi = -90°, -45°, 0, +45°, +90°$.) The NPS can be as low as two (i.e., a binary search within the PSR) and as high as allowed by the system hardware. A smaller NPS (i.e., coarse phase variations) produces a smaller number of power levels to be evaluated at the RU. This can result in a higher speed of operation and lower complexity in the detection at the expense of lower local accuracy, as shown in the example of Fig. 10. A smaller PSR would result in the exploration of a narrower subsection of all allowed phases. This usually (but not always) happens in the later iterations of the focusing, where the algorithm (through its automated operation) effectively performs fine-tuning of the phase settings. It can also be the case that volumetric refocusing (see Section V) is performed, and the main focusing algorithm performs a rapid final adjustment, using a smaller PSR.

One of the advantages of using orthogonal (or pseudo-orthogonal) masks is the smaller projection of optimization of one mask sweep on the other ones (theoretically zero for a perfectly orthogonal basis). The orthogonality enables the identification of the optimum phase (within the NPS) for different masks to be done in batch and independently without the need for constant updates to the GU setting after each mask. This can significantly reduce the number of communication updates from the RU to GU by using a longer CRL, which is the number of different RU power states reported back to the GU in one communication package. Using a complete mask set would enable getting closer to the optimum focusing with no blind spots in the optimization space.[28] An example of one such complete and orthogonal mask set is shown in Fig. 11 for a 4 × 8-array (or 4 × 8 segments within the array).
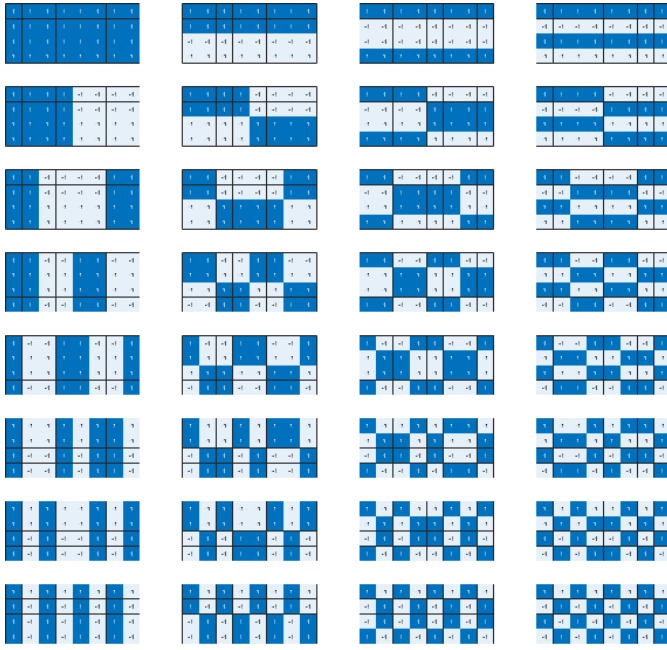
The mask-set of Fig. 11 is generated by multiplying columns of reordered H_4 (the 4 × 4 Hadamard matrix [36], [37]) by rows of reordered H_8 (the 8 × 8 Hadamard matrix). (More details of this 2-D mask generation using the Hadamard and pseudo-Hadamard matrices are discussed in the Appendix.) All these masks are orthogonal to each other, namely

$$\langle \mathbf{M}_i, \mathbf{M}_j \rangle = 0 \qquad i \neq j \qquad (17)$$

with the inner product definition of (16). In general, an orthogonal mask set of size $M \times N$ can be generated if H_M and H_N (Hadamard matrices of sizes $M \times M$ and $N \times N$) can be constructed either analytically or computationally. The individual masks are generated by doing a matrix multiplication

---

[28]In comparison, if a random selection of elements is used for the phase sweep, the system can be prone to incompleteness in its search, meaning that certain states or combinations of them may be missed or that more mask sets would need to be swept, potentially resulting in inferior performance compared with a well-chosen, non-random selection of elements.

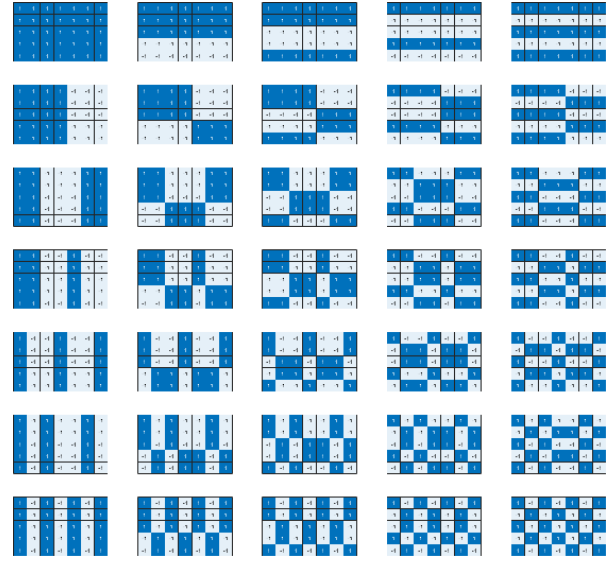Fig. 11.   Signed orthogonal mask set for a 4×8 array.

Fig. 12.   Signed pseudo-orthogonal mask set for a 5×7 array.

be as low as 1. The qualities of the mask-set and other system non-idealities (e.g., element coupling or pulling) determine the maximum useful value of the CRL.

of a column of the H_M matrix by a row of the H_N matrix to generate an $M \times N$-mask.[29]

If the Hadamard matrices do not exist for the desired M and N, pseudo-orthogonal mask sets can be constructed using the pseudo-Hadamard matrices introduced in the Appendix. An example of this is shown in Fig. 12 for a 5×7 mask-set. In this example, we have used pseudo-orthogonal $\hat{H}_5$ and $\hat{H}_7$ pseudo-Hadamard matrices.[30]

Using orthogonal or pseudo-orthogonal masks facilitates the evaluation of the optimum phases (and amplitudes) for multiple masks independently and sequentially without the need to update the GU phase setting after each phase sweep of the GU elements by the active mask. This can be particularly useful in the presence of large latency (e.g., for long-range systems) or bandwidth limitations (e.g., low power or passive communication) from RU to GU. The orthogonal and pseudo-orthogonal masks allow the phase sweeps to be done independently and the aggregate result effectuated in the GU after a predefined number of masks have been swept through. As we mentioned earlier, we call the number of masks swept between two communications from RU of the best power readout, CRL (measured in the number of masks), which can

B. Segmentation and Batch Processing

The mask sets do not need to be the same size as the full GU array. The array can be broken down into smaller segments, where, within each segment, a smaller set of (preferably orthogonal) masks will be used. For segments of size $M_s \times N_s$, there would only $M_s \times N_s$ masks. This will result in a smaller number of elements phase swept at any given time and fewer mask to sweep through, resulting in potentially faster sweeps, but at the cost of lower phase variation dynamic range. Fig. 13 shows an example of a 4×6 segmentation within a larger 16×12 array, where there will be 24 masks for each segment.[31]

The optimum phase setting for each mask within each segment is shown as $\Delta c_{\text{opt}}(i)$, corresponding to the binary code applied to the phase control element (e.g., the CMU) that produced the largest signal at the RU under the ith segment mask, $\mathbf{M}(i)$. For a CRL greater than 1, starting with mask n and going through CRL more masks, there would be the same number of the $\Delta c_{\text{opt}}(i)$ values. Once the CRL is reached and these individual values are communicated back to the GU, the new code settings are calculated by

$$\Delta \mathbf{C} = \mod \left(\sum_{i=n}^{n+\text{CRL}} \Delta c_{\text{opt}}(i) \mathbf{M}(i), \mathbf{P} \right) \qquad (18)$$

---

[29]The effect of this mapping can be seen in the variation of two elements phases, such as those shown in Fig. 6, where the individual phase changes correspond to the blue and red vectors, ϕ_1 and ϕ_2. The 2×1-orthogonal basis generated with the Hadamard matrixes corresponds to the masks: $\mathbf{M}_1 = [1, 1]$ and $\mathbf{M}_2 = [1, -1]$. These correspond (within a factor of 2) to common- and differential-mode signal projections in circuit vernacular and are shown as ϕ_c and ϕ_d in Fig. 6. An ascent performed in Fig. 6 using this new basis of ϕ_c and ϕ_d with 2π wrapping would eventually converge to the same global optimum point P_1, albeit through a different trajectory. The higher order basis, such as those shown in Figs. 11 and 12, provide more complex signal projections with higher signal variation dynamic range that allows the approach to overcome the noise.

[30]It should be noted that the orthogonal bases are not limited to those generated using the Hadamard matrices, and many other variations may exist. Also, the amplitude settings can be captured by similar mask-sets if necessary.

[31]It should be noted that the segments and elements themselves do not need to be physically collocated and that the designation of the elements themselves can also be arbitrary. For example, for a particular set of elements chosen (e.g., an orthogonal set), the physical location of any two elements can be interchanged, and the resulting set of elements may be preferred under certain circumstances. This process can be repeated on the resulting set without changing the property of these elements acting as a segment. Additional operations, such as row and column exchanges, rotations, and reflections, may also be applied. This also applies to nonuniform, sparse, non-planar, and mechanically changing arrays.
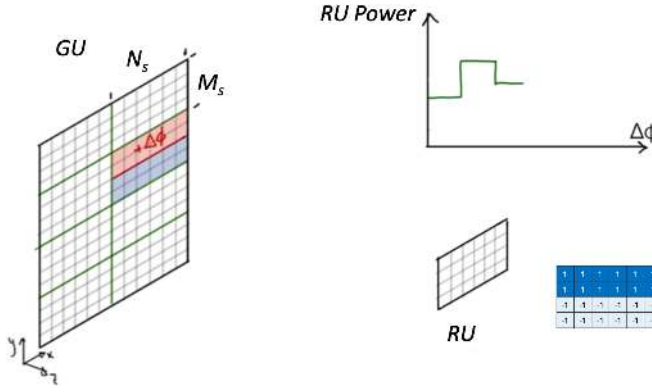
Fig. 13. Segmentation example of 4×6 $(M_s \times N_s)$ in a 16×12 $(M \times N)$ array.

where matrix **P**, called modulo here, captures the variations in the local phase control characteristics of individual phase synthesizers of each element. (e.g., if increasing the control word from 0 to 210 produces a monotonic phase advance of 2π, then $p_{ij} = 210$).

C. Iteration

The algorithm described is run in multiple iterations, where it adjusts its parameters dynamically to take advantage of direct tradeoffs between dynamic range and segmentation size, speed, and number and spacing of phase steps. The overall algorithm involves one or multiple iterations of this process, where the PSR, the NPS, the segmentation sizes $(M_s \times N_s)$, and the CRL can (and often do) change from one iteration to the next. For large initial PSR, greater variations in the phases of elements with respect to each other produce a large change in the received power in the RU. This larger dynamic range allows for the phases of a smaller number of elements to be changed in each step (smaller segment sizes). Typically, as the main loop progresses and the coarse phase tuning transitions toward finer tuning (smaller PSR), the variation in the amplitude becomes smaller, and larger segmentations would be advantageous as they would generate larger power variations in the RU.

The loop can start from a random initial state or use previously evaluated phase settings as a starting point to ensure faster convergence to the optimum phase setting.[32] The refocusing method of Section V in combination with inertial and other measures on the RU side can be used to rapidly calculate a new phase state to be used immediately or in conjunction with this algorithm (e.g., the algorithm starting from an intermediate iteration using those refocused values).

D. Interpolation

The algorithm has the option of using interpolation in between NPS + 1 phases in the range defined by PSR

[32]With sufficiently small focusing time, real-time RU tracking can be achieved, where the system dynamically refocuses at a sufficiently fast rate that the system effectively performs real-time RU tracking, and power transfer to the RU is never interrupted. We will discuss algorithms and methods enabling such solutions next.

Algorithm 1 Generalized Focusing Algorithm
───
$n_{comm} \leftarrow 1$
$\Phi_{best} \leftarrow \Phi_{init}$
$\texttt{GULoad}(\Phi_{best})$
for $i \leftarrow i_{min}$ **to** i_{max} **do**
  $[M_s, N_s] \leftarrow size_{seg}(i)$
  $\phi_{range} \leftarrow PSR(i)$
  $n_\phi \leftarrow NPS(i)$
  $crl \leftarrow CRL(i)$
  $maskset \leftarrow \texttt{MaskGen}(M_s, N_s)$
  for $n_{mask} \leftarrow 1$ **to** $M_s \cdot N_s$ **do**
    $mask \leftarrow maskset(n_{mask})$
    for $seg \leftarrow 1$ **to** $(M \cdot N)/(M_s \cdot N_s)$ **do**
      for $\phi \leftarrow 0$ **to** ϕ_{range} **step** ϕ_{range}/n_ϕ **do**
        for $r \leftarrow 1$ **to** M_s **do**
          for $c \leftarrow 1$ **to** N_s **do**
            $\Phi(r, c) \leftarrow \texttt{mod}(\Phi_{best}(r, c) + \phi \cdot$
            $mask(r, c), modulo(r, c))$
          end
        end
        $\texttt{GULoad}(\Phi)$
        $GU_{hist}(n_{comm}) \leftarrow [\phi, seg, n_{mask}]$
      end
      if $n_{comm} = crl$ **then**
        $RU_{hist} \leftarrow \texttt{RURead}()$
        for $j \leftarrow 1$ **to** crl **do**
          for $r \leftarrow 1$ **to** M_s **do**
            for $c \leftarrow 1$ **to** N_s **do**
              $\Phi_{Best}(r, c) \leftarrow$
              $\texttt{mod}(\Phi_{best}(r, c) + \phi(RU_{hist}(j)) \cdot$
              $mask(GU_{hist}(j)), modulo(r, c))$
            end
          end
        end
        $\texttt{GULoad}(\Phi_{best})$
        $n_{comm} \leftarrow 1$
      end
      else
        $n_{comm} \leftarrow n_{comm} + 1$
      end
    end
  end
end
───

within each sub-iteration. It finds the best phase by fitting the measured power pattern to the appropriate sine and cosine functions to identify the best phase setting within that range. This phase is often between the actual tested points and does not exactly correspond to one of them. This option often leads to faster convergence, less sensitivity to single-events, and higher final power values.

E. Pseudo-Code

A simplified example of the high-level pseudo-code of the algorithm is shown as Algorithm 1.
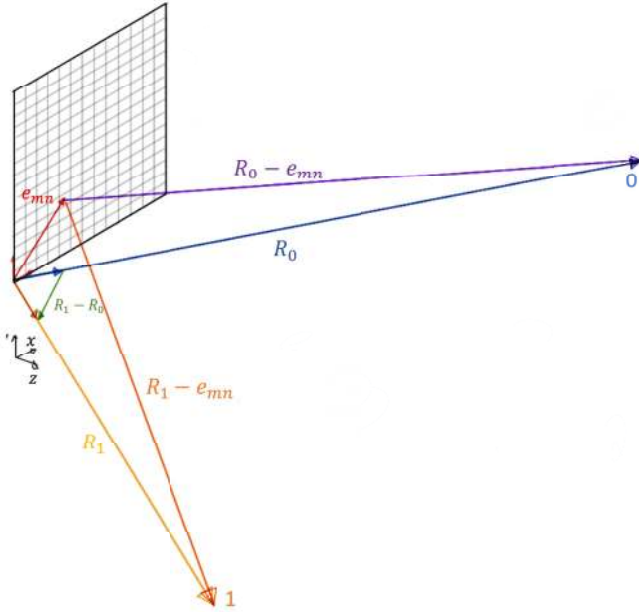
Fig. 14. Coordinate system for refocusing.

V. SECONDARY VOLUMETRIC REFOCUSING

It is highly desirable for an RF lensing system to be able to rapidly refocus the energy on a different arbitrary point in the 3-D-space in both near- and far-field regions, something that traditional beam-forming approaches are not typically intended for.[33] This is useful in many applications, such as dynamic tracking of an RU in a WPT-AD system, real-time mapping of the space (e.g., within a room) for imaging and sensing, or high-efficiency data communication. The secondary dynamic volumetric refocusing eliminates the need for multiple potentially time- and energy-consuming primary focusing attempts (e.g., the method of Section IV). Instead, it refocuses in 3-D using a rapid calculation of new coefficients based on a single primary focus at a known location.[34]

As a starting point, consider the case of a regular rectangular $M \times N$ array, where each element has an arbitrary and unknown random phase offset (e.g., because of the different path lengths for low-frequency reference distribution lines). Assume that the focusing algorithm has already been used to maximize power at point **0** with known coordinates $R_0 = (x_0, y_0, z_0)$ with reference to the array origin in Fig. 14 (lower left corner here). It is now desirable to be able to refocus on point **1** located at $R_1 = (x_1, y_1, z_1)$.

Vector e_{mn} captures the location of an arbitrary element with indexes m and n within an arbitrary array. In a regular array, it can be expressed as

$$e_{mn} = (md_x\hat{i} + nd_y\hat{j})$$
$$|e_{mn}|^2 = (d_x^2\, m^2 + d_y^2\, n^2)$$

[33]It subsumes far-field beamforming by focusing on points at infinity.

[34]Information about this new location can be obtained from other sensors, such as inertial measurements that, in conjunction with other inputs to the system, can be used to estimate the new location of the RU. This estimate does not need to be exact, and the focusing can further be refined by the algorithms of this and Section IV.

where d_x and d_y are element spacings in the x- and y-directions. Note that there is no need for a square or even a regular array as long as e_{mn} is known since tracking is done on a per element basis. This allows for independent operation and independent formation of multiple focal points using different segments of the array if necessary.

The path length difference in conjunction with phase differences between different elements in the array is what is responsible for focusing. In Fig. 14, the path length difference for two elements, from one at the origin $(0, 0)$ and one at e_{mn}, to a location described by any given vector R is given by

$$\Delta l_{mn}(R) = |R - e_{mn}| - |R|$$
$$= [|R|^2 - 2R \cdot e_{mn} + |e_{mn}|^2]^{\frac{1}{2}} - |R|. \quad (19)$$

The phase difference between the signals at location **0** generated by the two elements located at the origin and the one at $|e_{mn}|$ is given by

$$\Delta\phi_{mn,0} \stackrel{2\pi}{\equiv} \phi_{mn,0} - \phi_{00,0}$$
$$\stackrel{2\pi}{\equiv} \frac{2\pi}{\lambda}\Delta l_{mn}(R_0) + \psi_{mn,0} - \psi_{00,0} \quad (20)$$

where $\phi_{00,0}$ and $\phi_{mn,0}$ are the phases of the signals generated by the elements at the origin and at e_{mn}, respectively. Variables $\psi_{00,1}$ and $\psi_{mn,1}$ express the generally unknown excess phase offset of the elements at the origin and e_{mn}, respectively. The symbol $\stackrel{2\pi}{\equiv}$ represents a modulo-2π equivalence for phase (phase wrapping).

Similarly, the phase shift due to those two elements at a new location, **1**, can be expressed as

$$\Delta\phi_{mn,1} \stackrel{2\pi}{\equiv} \phi_{mn,1} - \phi_{00,1}$$
$$\stackrel{2\pi}{\equiv} \frac{2\pi}{\lambda}\Delta l_{mn}(R_1) + \psi_{mn,1} - \psi_{00,1}. \quad (21)$$

Now, to focus at location **1**, the phase difference $\Delta\phi_{mn,0}$ has to be an integer multiple of 2π and similarly for $\Delta\phi_{mn,1}$, i.e.,

$$\Delta\phi_{mn,0} \stackrel{2\pi}{\equiv} \Delta\phi_{mn,1} \stackrel{2\pi}{\equiv} 0. \quad (22)$$

Using this congruence relation allows phase recalculation at the individual element level for any new refocusing location based on a single original focus at a known location (R_0 here). To achieve this, we can solve for the necessary phase of the element at e_{mn} with respect to the element at the origin, namely

$$\Delta\psi_{mn,1} = \psi_{mn,1} - \psi_{00,1}$$
$$\stackrel{2\pi}{\equiv} \Delta\phi_{mn,1} - \frac{2\pi}{\lambda}\Delta l_{mn}(R_1)$$
$$\stackrel{2\pi}{\equiv} \frac{2\pi}{\lambda}[\Delta l_{mn}(R_0) - \Delta l_{mn}(R_1)] + \Delta\psi_{mn,0} \quad (23)$$

which leads to a simple expression for the necessary phase shift setting at the GU between elements at the origin and the one at e_{mn}

$$\Delta\psi_{mn,1} \stackrel{2\pi}{\equiv} \Delta\psi_{mn,0} + \frac{2\pi}{\lambda}[\Delta l_{mn}(R_0) - \Delta l_{mn}(R_1)]$$
$$\stackrel{2\pi}{\equiv} \Delta\psi_{mn,0} + \frac{2\pi}{\lambda}\Delta L_{mn}(R_0, R_1) \quad (24)$$

where $\Delta L_{mn}(\boldsymbol{R_0}, \boldsymbol{R_1})$ is the path length difference for the element at $\boldsymbol{e}_{mn}$ with respect to the element (the origin) for target points $\boldsymbol{R_0}$ and $\boldsymbol{R_1}$, which can be computed as

$$\Delta L_{mn}(\boldsymbol{R_0}, \boldsymbol{R_1}) = [|\boldsymbol{R_0}|^2 - 2\boldsymbol{R_0} \cdot \boldsymbol{e}_{mn} + |\boldsymbol{e}_{mn}|^2]^{\frac{1}{2}}$$
$$- [|\boldsymbol{R_1}|^2 - 2\boldsymbol{R_1} \cdot \boldsymbol{e}_{mn} + |\boldsymbol{e}_{mn}|^2]^{\frac{1}{2}}$$
$$+ |\boldsymbol{R_1}| - |\boldsymbol{R_0}|. \tag{25}$$

It is noteworthy that the element-wise correction removes the random phase offset. When the element phase shift is generated using a digital word fed to an element phase synthesizer (e.g., the clock multiplier unit (CMU) in Section VI), the relationship between the induced phase, ψ_{mn}, and the phase synthesizer control word is generally nonlinear and has arbitrary offsets that change from element to element

$$\psi_{mn} = \psi(C_{mn}) \tag{26}$$

which can be approximated as a linear relationship

$$\psi_{mn} = a_{mn}C_{mn} + b_{mn} \tag{27}$$

where a_{mn} is the slope of the linear fit and b_{mn} is the random offset that can assume any arbitrary value due to reference skew. Using the linear approximation, we can obtain

$$\Delta \psi_{mn,1} \stackrel{\frac{2\pi}{\lambda}}{\equiv} \Delta \psi_{mn,0} + \frac{2\pi}{\lambda}\Delta L_{mn}(\boldsymbol{R_0}, \boldsymbol{R_1})$$
$$\stackrel{\frac{2\pi}{\lambda}}{\equiv} a_{mn}C_{mn,1} + \cancel{b_{mn}} - (a_{00}C_{00,1} + \cancel{b_{00}})$$
$$\stackrel{\frac{2\pi}{\lambda}}{\equiv} a_{mn}C_{mn,0} + \cancel{b_{mn}} - (a_{00}C_{00,0} + \cancel{b_{00}}) + \frac{2\pi}{\lambda}\Delta L_{mn}. \tag{28}$$

Canceling b_{mn} and b_{00} between the second and third parts of (28), we obtain

$$a_{mn}(C_{mn,1} - C_{mn,0}) \stackrel{\frac{2\pi}{\lambda}}{\equiv} a_{00}(C_{00,1} - C_{00,0})$$
$$+ \frac{2\pi}{\lambda}\Delta L_{mn}(\boldsymbol{R_0}, \boldsymbol{R_1}). \tag{29}$$

We can *define* $C_{00} = 0$ for all settings without loss of generality. Thus, $C_{00,1} - C_{00,0} = 0$, and the change in the phase synthesizer code for the individual element at $\boldsymbol{e}_{mn}$ should be

$$\Delta C_{mn} = (C_{mn,1} - C_{mn,0})$$
$$\stackrel{\frac{2\pi}{a_{mn}}}{\equiv} \frac{2\pi}{a_{mn}} \cdot \frac{\Delta L_{mn}(\boldsymbol{R_0}, \boldsymbol{R_1})}{\lambda}. \tag{30}$$

The $M \times N$-matrix $\Delta L_{mn}(\boldsymbol{R_0}, \boldsymbol{R_1})$ states the shift in the code word of the phase synthesizer for each element and can be calculated only once for any new location *at the element level*. This local calculation is computationally efficient. It can also be applied in nonuniform and sparse arrays. It can be also cached in memory and does not need to be recalculated every time.[35]

---

[35]It should be noted that the effectiveness of the refocusing approach may diminish to some extent in strongly scattering environments due to multipath. However, this effect is less pronounced in wireless power transfer compared with communication systems due to the more directional nature of the transmission.
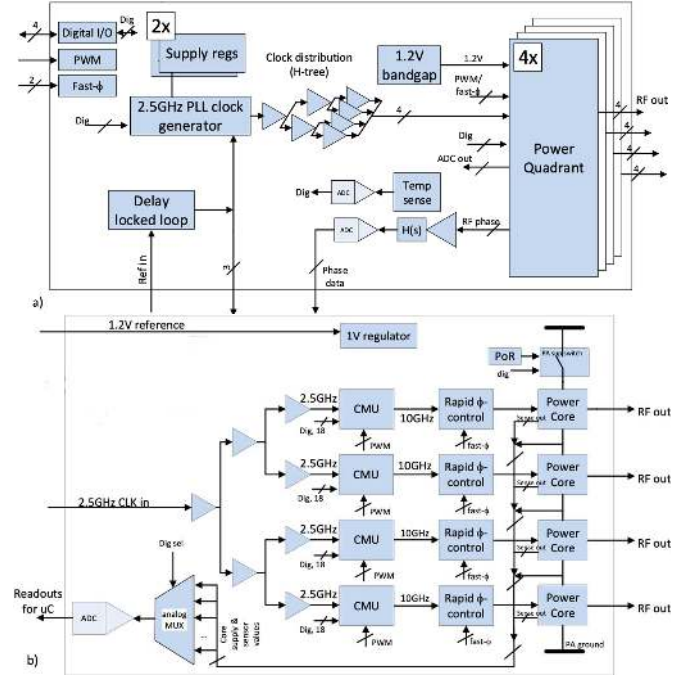

Fig. 15. (a) Top-level RFIC with 16 independently controlled RF outputs. (b) Detailed architecture of each power quad. [16].

VI. HARDWARE PLATFORM

While the system is not limited to any specific frequency, there are fundamental advantages for operating at higher operation frequencies, as discussed in Section II-F. The system size, range, and focusing capability significantly improve with higher frequencies. However, the drawbacks of the operation in mm-wave and higher microwave frequencies are the higher system complexity, parameter sensitivity, component density, and cost. This makes it very difficult to realize a reliable and economical system using discrete and commercial off-the-shelf (COTS) components and naturally leads to an integrated CMOS RFIC solution [28]. In this section, we describe the design of a single-chip CMOS IC that integrates all the components of an array building block with the ability to synthesize and amplify multiple independently controlled RF outputs at 10 GHz from a low-frequency reference signal.

A. IC Architecture

By integrating the functions of frequency synthesis, phase and amplitude control, power generation, and regulated operation for multiple radiators on a single RFIC system-on-chip (SOC), a truly modular scalable solution can be obtained, as shown in Fig. 15. Each RFIC independently controls the phase and amplitude of 16 different outputs (radiators), and multiple RFICs are synchronized to a single reference signal [38] to form a highly scalable system.

Each chip utilizes 17 on-chip PLLs performing a two-step RF power generation. The on-chip central, programmable PLL in Fig. 15(a), whose details can be seen in Fig. 16, synthesizes a 2.5-GHz RF signal from a low-frequency (5–200 MHz) external reference clock that is distributed to different RFIC
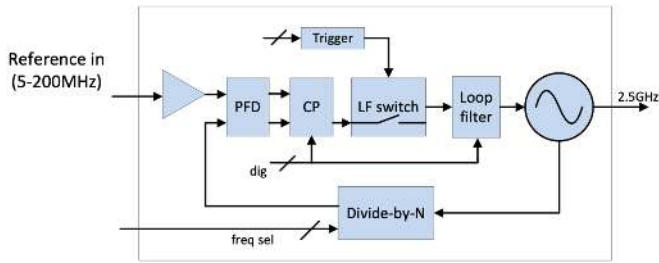
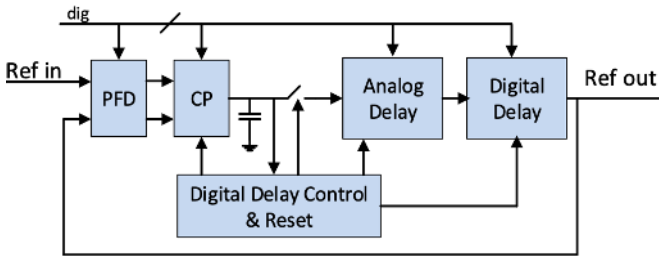Fig. 16. First programmable frequency synthesizer for the internal 2.5-GHZ reference generation.

Fig. 17. Reference redistribution DLL.

Fig. 18. One of the 16 CMU PLLs with 4× frequency multiplication and phase control through digital code.

units. This approach allows the distribution of a lower frequency (2.5 GHz) reference across the chip to 16 different locations in order to mitigate the loss and dispersion issues. The chip also utilizes buffers and delay-locked loop (DLL) circuitry [39] to allow retiming and redistribution of the low-frequency reference between chips (see Fig. 17). This is crucial when large arrays scale to sizes where it is impractical to use a single central clock source to directly drive all the system RFICs.

The 2.5-GHz reference is distributed on-chip to four groups (quadrants) of four independently controlled RF chains [see Fig. 15(b)]. Each of the four chains within a quadrant employs a second CMU to synthesize an output signal around 10 GHz. The CMUs also operate as programmable phase synthesizer by introducing a digitally controlled current offset to the multiplier charge pumps, as shown in Fig. 18. The implemented current DAC (IDAC) is an 8-bit thermometer-coded IDAC that can add or subtract current from the PLL loop filter. The use of thermometer-coded architecture insures monotonic phase change with respect to the input phase code. In a WPD-AD system that utilizes TDM to power multiple devices at the same time, simultaneous phase updates are required to reduce the dead time overhead between the beamswitching. The CMUs incorporate four phase register banks that can enable up to four TDM slots. Rising edges on a PWM signal will simultaneously update the phase of all elements in the array by connecting the next register bank to the IDAC. The width of the PWM signal defines the duration of beam dwell time and enables simple power allocation control. Introducing a phase shift through the CMU is simple and efficient. However, it requires stabilization of the feedback loop and might be too slow for certain applications. Thus, the CMUs are followed by fast vector modulators [40] capable of phase and amplitude control, as shown in Fig. 15(b). The combination of the slow-but-accurate CMU phase control, with the fast
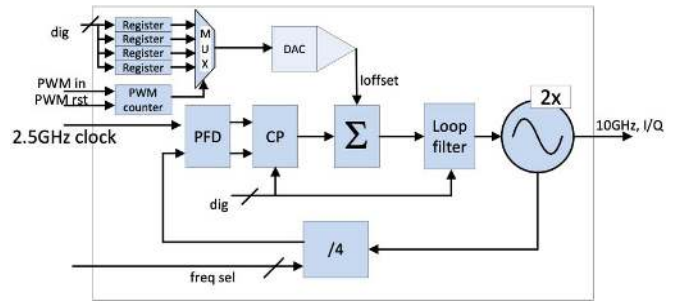
phase-and-amplitude vector modulator, provides the option to modulate high-speed data constellations while maintaining focusing (and other RF-lensing operations) through carrier phase coherence enforced by the CMU.

The fast vector modulators include local pre-programmable phase and amplitude settings through lookup tables (LUTs) implemented using static random access memory (SRAM) with settings that can be loaded into the rapid phase controlling circuits through an address register. In addition, the address register itself can also be incremented and controlled through a global, 1-bit control line that triggers a counter to load the next address into the register. This functionality allows the system to rapidly switch between pre-programed focal points to accelerate servicing multiple RUs for TDM power distribution, other clients, or additional system functionality. Random memory access allows pre-loading data such that exhaustive raster or other scans of arbitrary resolution using different beams can be implemented. Finally, the single-bit control line can be pulsewidth modulated to control beam dwell times at different physical locations. As the local SRAM can operate at very high speeds, the transition time between beam settings can be kept to a minimum.

In order to reduce on-chip coupling and crosstalk, supply domains between quadrants and within a quadrant are separated and individually controlled using programmable on-chip linear supply regulators. Internal supply rail voltages and output from additional sensors can be digitally read using on-chip DACs, as seen in Fig. 15(b).

Each chain is completed by a power generation block, as shown in Fig. 19 (16 in total). Each RF chain PA can be operated and controlled independently. However, within each quadrant, they are stacked from a dc perspective, as illustrated in Fig. 20. This allows for reuse of the current that is shared by the four cores in order to bias the PAs at four times higher voltage and significantly reduce IR drops on the supply lines. A control algorithm is used to monitor and adjust the operating voltages of the amplifiers dynamically [38]. The final stage of each amplifier, where most of the dc-to-RF power conversion occurs, is realized using a differential cascode to guarantee reliability under load mismatch, as shown in Fig. 21.

B. GU Architecture

The self-contained RFIC in Fig. 22(a) is the centerpiece of a unit building block daughter card for the modular system.
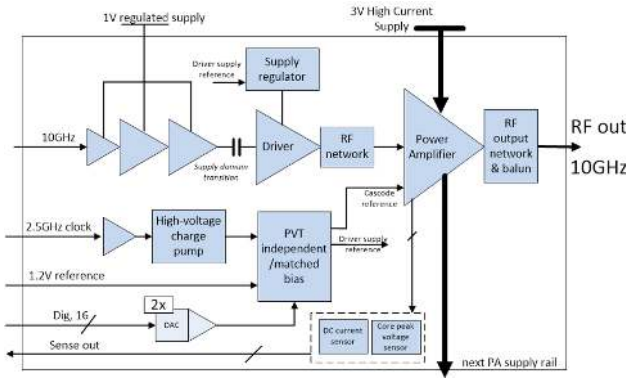
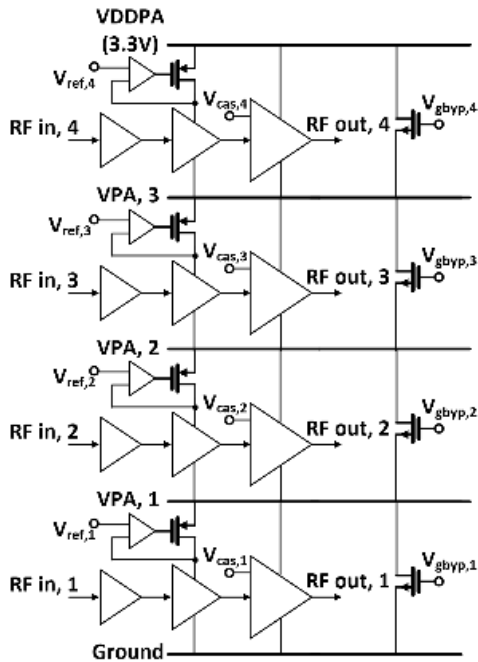Fig. 19.   Power generation chain details.

Fig. 20.   Details of the four-PA stack within each power quadrant.

Each daughter card incorporates eight dual-polarized radiators in a 2×4-grid, where two separate RFIC outputs drive two polarization-ports of each radiator, as seen depicted in Fig. 24(b). Various size systems can be rapidly assembled using low-frequency motherboards of various sizes, as seen in Fig. 22(c). The power supply, shared reference clock, and programming interface are distributed to all the array's tiles via the motherboard, with the principles of scalable array architecture set out in [41]. The element spacing is 16.5 mm (0.55λ), and arrays of varying size and shape can be quickly assembled using different numbers of daughter cards. The algorithm is run centrally, and the phase information of the RFIC digital registers is updated in each iteration.[36]

[36]Each step of the iteration on the GU involves reprogramming new phase setting of some of the elements digitally through ten independent SPI interfaces running at 2 Mb/s (for a total of 20 Mb/s), where a central 48-MHz micro-controller runs the algorithm and updates the phase settings of the RFICs. At this rate, up to 6250 full-size (20×20) mask iterations can be programed into the GU in the 400-element prototype. This is also assuming that focusing is constantly running, which is far from the actual physical scenarios.
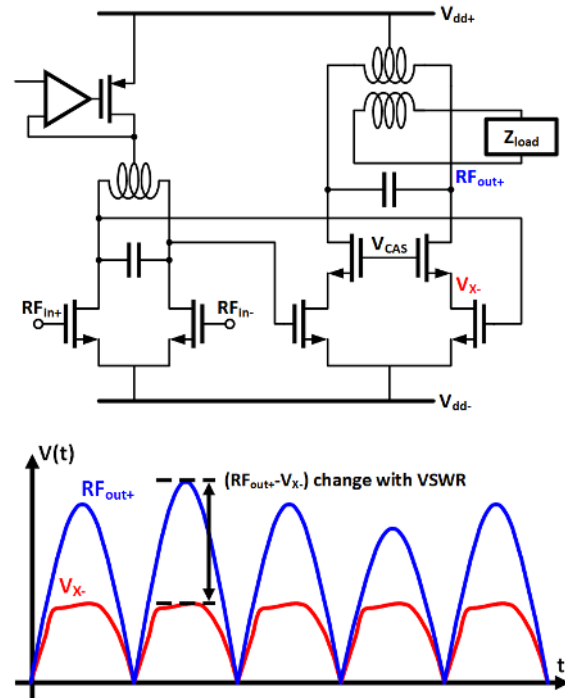

Fig. 21.   Output RF stage details and the associated waveforms.

This architecture enables very large and highly scalable arrays, using a large number of silicon RFICs. The small component-count, predictability, and repeatability of manufactured parts and feature-rich functionality make it economically attractive for a wide range of commercial applications. Several generations of the system have been constructed at different frequencies, as shown in Fig. 23, where the impact of the frequency choice on the system size is quite pronounced.

As a comparison, conventional beam-forming and scanning phased arrays [5] try to uniformly distribute an internal RF source and use in-line phase shifters to introduce additional phase shifts. These phase shifts are then adjusted to form and redirect a beam focused at infinity to the new direction known in advance. One of the advantages of low-frequency reference distribution and local high-frequency synthesis is the lower power consumption associated with the reference distribution network and the ability to use more standard PCB materials and fabrication processes for reference distribution. The architecture proposed here can tolerate very large[37] delay variations among various daughter cards due to low-frequency reference distribution length variations, as well as different transmission line lengths leading to the individual antennas, as shown in Fig. 24. The delay can result from manufacturing variation, routing constraints, and board-level RF interference and manifests as an absolute phase shift between radiating elements. Furthermore, as is the case with other reference distribution techniques, it is also prone to temperature and environmental variations. For example, at 10 GHz, where a typical electrical length on a daughter card is about 1.5 cm, routing differences of 1 mm translate into a phase mismatch of more than $\lambda/8$. In a large array, the initial phase differences

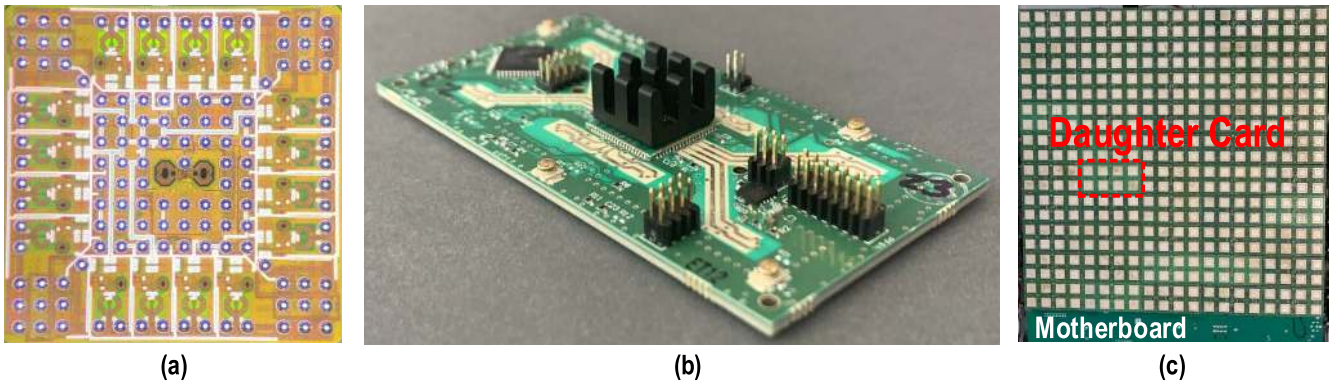[37]Theoretically unlimited (subject to signal loss).

Fig. 22. (a) RFIC die photograph. (b) 2×4 array tile. (c) 32 tiles, 256-elements array at 10 GHz.
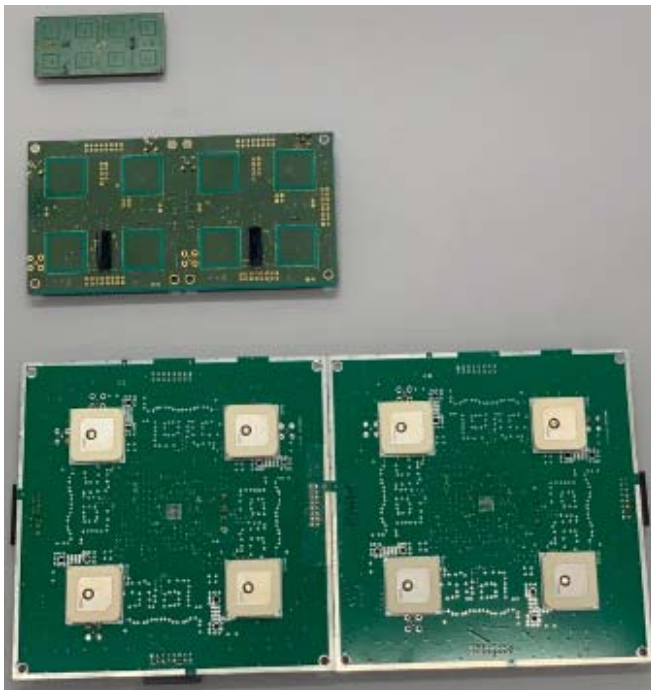

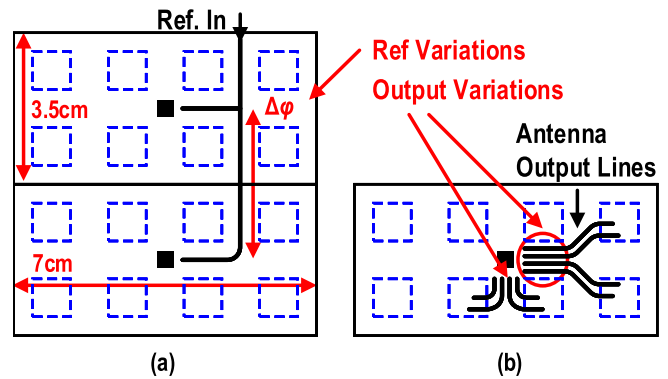Fig. 23. Designed and manufactured 2×4 GU building block at 10, 5.8, and 2.45 GHz.

Fig. 24. Length variations due to (a) reference distribution routing and (b) output antenna traces at 10 GHz.

between outputs can be practically random, necessitating a focusing approach that is insensitive to this randomness and can handle the phase differences. This was discussed extensively in Sections III and IV.

C. RU Architecture

RUs play an important role in the system, as each RU captures the incident RF signal, converts it to dc to drive a load, and provides periodic wireless feedback to the GU about the received power status and its need for power. A typical RU uses an array of antennas, which couples the incident wave into its port(s). Unlike classical phased array communication receivers that form a narrow listening beam by combining the RF power from multiple antennas coherently and controlling the listening direction through phase (delay) adjustments, an ideal RU should present a large aperture and

a large field of view (FOV) at the same time. This seemingly impossible tradeoff can be overcome by using nonlinear and/or multi-mode antennas [42].

An alternative method for wireless power transfer is to directly couple each antenna[38] to a rectifying element[39] also tuned to the desired frequency and power range. The dc output power of these elements can be combined directly.[40]

This approach allows the aperture of the RU[41] to be accessible at a wide FOV without element-wise phase alignment. The rectification is a nonlinear process. Modeling the rectification process as a simplified squaring process, the RF signal is down-converted to baseband (dc) by serving as its own LO. As a result, each element is automatically down-converted with the correct phase shift and combined at dc, which is the only frequency at which all signals are, by definition, in phase.

The RF rectifiers' power flow (RF to dc) is the inverse of those of the PAs (dc to RF). This makes it possible to apply the PA design insights to it [43]. A harmonically terminated Schottky diode rectifier can benefit from waveform engineering techniques used in PA design to achieve better performance [44].

---

[38]Or a cluster of antennas.

[39]The combination is sometimes referred to as a rectenna for rectifying antenna.

[40]It is also possible to combine the outputs of multiple dc-to-dc converters for better performance.
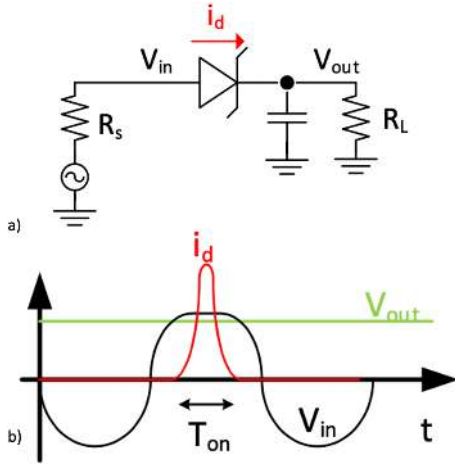
[41]Scaled by the element pattern.

Fig. 25. Conceptual (a) schematic of a simple diode rectifier and (b) corresponding voltage and current waveforms.

Fig. 25 shows a basic RF rectifier and the conceptual voltage and current waveforms for a simplified static diode model (open in reverse and linear resistor in forward with no capacitance). For optimum conversion, the ratio of the dc loss in the diode to the input delivered power should be minimized. In this simplified model, the diode power loss P_{loss} is

$$P_{\text{loss}} = \frac{1}{T} \int_{T_{\text{ON}}} V_d I_d dt \approx \frac{1}{T} \int_{T_{\text{ON}}} (V_{\text{ON}} + I_d R_d) I_d dt$$
$$= \frac{V_{\text{ON}}}{T} \int_{T_{\text{ON}}} I_d dt + \frac{R_d}{T} \int_{T_{\text{ON}}} I_d^2 dt \tag{31}$$

where I_d is diode current, R_d is the diode series resistance, V_{ON} is the intrinsic turn-on voltage of the diode, T_{ON} is the period over which the diode conducts, and T is the full period. The diode current replenishes the charge lost in the capacitor each cycle; hence

$$\int_{T_{\text{ON}}} I_d dt = I_L T \tag{32}$$

where $I_L = V_{\text{out}}/R_L$ is the load current. The second term in (31) is the ohmic loss of the diode, which is proportional to the mean square average of the current. Using the following inequality:

$$\frac{1}{T_{\text{ON}}} \int_{T_{\text{ON}}} I_d^2 dt \geq \left(\frac{1}{T_{\text{ON}}} \int_{T_{\text{ON}}} I_d dt \right)^2 \tag{33}$$

and substituting (32) into (31), we obtain

$$P_{\text{loss}} \geq V_{\text{ON}} I_L + R_d I_L^2 \frac{T}{T_{\text{ON}}}. \tag{34}$$

The conversion efficiency of the rectifier can be expressed as

$$\eta_c = \frac{P_{\text{out}}}{P_{\text{acc}}} = \frac{P_{\text{out}}}{P_{\text{out}} + P_{\text{loss}}} = \frac{V_{\text{out}} I_L}{V_{\text{out}} I_L + P_{\text{loss}}}$$
$$\leq \frac{V_{\text{out}}}{V_{\text{out}} + V_{\text{ON}} + I_L R_d \frac{T}{T_{\text{ON}}}} \tag{35}$$

where V_{out} is the output dc voltage. It should be noted that the equality holds if and only if I_d is constant over T_{ON}.
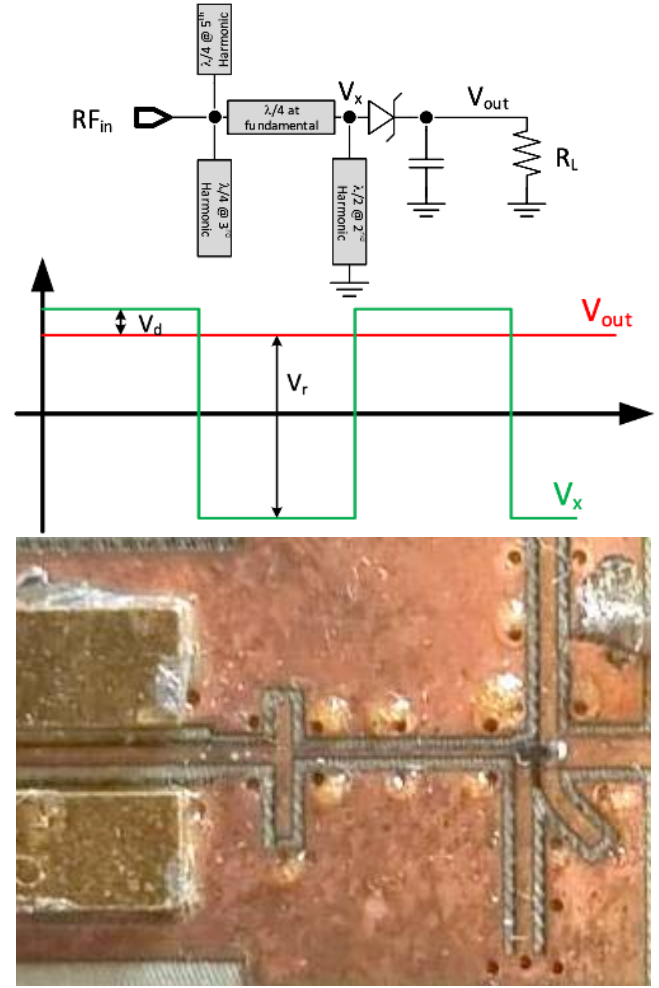

Fig. 26. (a) Block diagram of the proposed harmonic termination for the rectifier. (b) Idealized voltage waveforms. (c) Fabricated 10-GHz rectifier.

Constant I_d forces constant V_{in} over the on period of the diode. From (35), we deduce that increasing T_{ON} will increase the efficiency. This is why square waveforms of a class-F type harmonic termination of the type shown in Fig. 26 are desirable for rectification applications.

The optimum performance can be obtained for maximum V_{out} and also when the current passing through the diode is small enough such that the voltage drop in the series resistance of the diode is negligible. Based on Fig. 26, the following relation between V_{out}, V_d, and the reverse voltage on the diode, V_r, is held at:

$$V_{\text{out}} = \frac{V_r + V_d}{2} - V_d = \frac{V_r - V_d}{2}. \tag{36}$$

Hence, the maximum output voltage that can be achieved is when the diode is close to the breakdown voltage: $V_{\text{out,max}} = (V_{r,\text{max}} - V_d)/2$. As a result, the maximum efficiency of a diode rectifier cannot exceed

$$\eta_c \leq \frac{V_{r,\text{max}} - V_{\text{ON}}}{V_{r,\text{max}} + V_{\text{ON}}} = \frac{1 - \frac{V_{\text{ON}}}{V_{r,\text{max}}}}{1 + \frac{V_{\text{ON}}}{V_{r,\text{max}}}} \approx 1 - 2\frac{V_{\text{ON}}}{V_{r,\text{max}}}. \tag{37}$$

To approach this limit in (37), the input RF voltage swing, which is the fundamental component of the square wave shown

in Fig. 26, should be $2/\pi \cdot (V_{r,\max} + V_{ON})$. This way, the diode is driven close to breakdown voltage, while the RF current should be small enough that the voltage drop across the diode does not become comparable to the diode turn-on voltage.[42]

The block diagram of the proposed rectifier is shown in Fig. 26. The diode is placed in series, and the anode is connected to the RF side, while the cathode is connected to the dc side. This allows for low capacitance loading of the RF side as the metal contact in the *n*-type Schottky diode forms the anode and has a smaller parasitic capacitance compared with the cathode, which is formed on the semiconductor substrate. The rectifier utilizes a class-F matching network to shape the waveforms and block the harmonics from reflecting back to the source. The anode of the Schottky diode is connected to a $\lambda/2$ short stub at the second harmonic. This stub provides a short impedance at the second harmonic and close to the short impedance at higher-order even harmonics, thus preventing the generation of even harmonics at the anode of the Schottky diode. At the fundamental frequency, the stub is close to $\lambda/4$ and will act as an open. It also provides the dc current path for the rectifier. The $\lambda/4$ open stubs at the third and fifth harmonics prevent these odd harmonics from radiating back to the RF source, hence improving the efficiency. The $\lambda/4$ line at the fundamental between these open stubs and the anode of the diode assures that these stubs appear as open at the third and fifth harmonics at the anode of the diode and, hence, do not block the generation of those harmonics. Consequently, the waveform on the diode can be very close to a square wave as a class-F network requires. At the fundamental frequency, however, these stubs have a capacitive reactance, and after the $\lambda/4$ transformation, they will have an inductive reactance on the anode of the diode. By adjusting the width of these stubs, they can be made to resonate with the parasitic capacitance of the diode.

A dual-polarized patch antenna was designed, and a rectifier was placed at each port, where the two cross-polarization components of the incident wave are independently rectified. In its simplest reincarnation, the power from all elements within a given polarization is combined directly in dc and drive a boost converter as a load. The use of both polarizations provides axial rotation angle independence for the RU. A low-power transceiver is used to transmit the batches of the measured rectified voltage levels back to the GU.[43] The front and back images of an RU array are shown in Fig. 27.

VII. EMULATOR

A modular emulator for the system discussed in Section VI is developed to assess its behavior under various physical configurations, system parameters (such as noise, coupling, and element EM propagation properties), and algorithm settings.

[42]If the diode's series resistance is large, this implies a large RF source impedance. In practice, matching network losses and the limited Q factor of the parasitic capacitance/inductance of the diode degrade the performance. It is possible to get close to this maximum value using a diode with low resistance and parasitic capacitance.

[43]Each measurement result can be captured as a byte of data, which, for 500 iterations, translates to less than a kB/s, a very low communication overhead for the system.
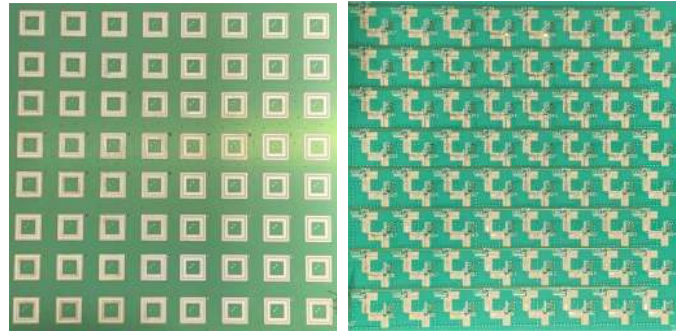

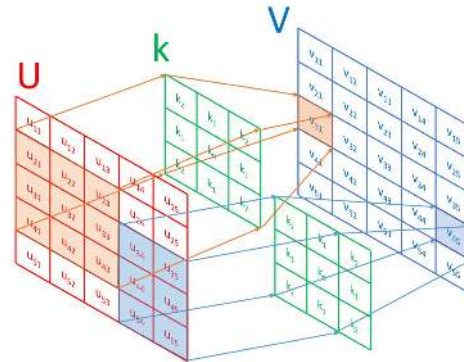Fig. 27. Front and back sides of one example implementation of the RU array.

Fig. 28. Relationship between the intended phases (and amplitude) **U** and the effective radiated fields, **V**, due to coupling captured by **k** through a moving 2-D convolution.

It consists of independently programmable modules for the GU(s), the RU(s), EM propagation, and the algorithm, where each accounts for non-idealities within their domains.

A. GU Emulator Module

The GU model accounts for a variety of GU non-idealities. It provides a model for the randomness of initial fixed phase offsets in the elements due to varying reference distribution lengths discussed in Section VI. It also allows for adjustment of various geometric properties of the GU (size, element spacing, and so on).

The GU emulator module also models both amplitude and phase noise of the active devices. Different SNR values for the noise sources can be chosen to model the physical system more accurately. It can also account for linear and nonlinear couplings of adjacent elements. The linear coupling can be modeled using matrix $\mathbf{S}_{GU}$ in (1), which can be either directly obtained through a one-time EM simulation of the GU radiator array (or its subsections) or estimated using the simplified coupling model.

In a GU with $G = MN$ equally spaced elements, the radiating array is driven with given phases and amplitudes presented as the complex matrix **U**. However, the radiated electric field at the output of the elements will, in general, be a different complex matrix **V** due to the element coupling. The signal coupling between adjacent elements can happen through various mechanisms at different levels (such as chip- and board-level non-radiative and radiative couplings, with or with

scattering). All these linear coupling mechanisms can be taken into account using an aggregate complex coupling matrix $\mathbf{k}$, also known as the kernel.[44] The effective coupled output $\mathbf{V}$ is

$$\mathbf{V} = \mathbf{k} * \mathbf{U} \tag{38}$$

where $*$ represents the matrix convolution of the coupling kernel, $\mathbf{k}$, and the intended drive $\mathbf{U}$. An example of $\mathbf{U}$ and $\mathbf{V}$ is shown in Fig. 28. The GU-module calculates the coupling kernel, $\mathbf{k}$, from the individual coupling properties using proper linear algebra operations. The conservation of energy considerations leads to the following constraint:

$$\langle \mathbf{V}, \mathbf{V} \rangle \leq \langle \mathbf{U}, \mathbf{U} \rangle. \tag{39}$$

The emulator ensures that this constraint is satisfied by optimizing the phases of $\mathbf{U}$ to maximize $\langle \mathbf{V}, \mathbf{V} \rangle$ and then normalizing $\mathbf{k}$ by this value.[45]

B. RU Module

The goal of the RU module is to calculate the total received power from the fields coupled into each element. The RU can be modeled as an array with R elements and fixed element spacing. The RU module takes into account the effect of added noise at the RU, the quantization noise, and the averaging effects of analog-to-digital conversion at the RU. It can also account for nonlinear reception and/or rectification behavior, as well as various other non-idealities, such as EM and thermal coupling.

C. Electromagnetic Propagation Module

The propagation module takes geometric parameters of the GU and RU system (size, arrangement, orientation, and placement) and the EM radiation patterns of the radiating elements within the array and uses the methodology of Section II to estimate the $G \times R$-coupling matrix and $\hat{\mathbf{S}}$ sub-matrix of (1). For a given stationary configuration, this remains fixed and, thus, needs to be calculated only once.

D. Algorithm Module

The algorithm module allows different algorithms and settings to be evaluated under various physical configurations by calling on the remaining modules to evaluate the response to various GU settings on the output. It accounts for various non-idealities, such as latency and batch data communication.

E. Emulator Results

The amplitude and phase noise in the GU and the noise in the RU result in a random trajectory toward the final focusing state. This is visible in the representative plots of Fig. 29, where the individual effect of the noise on the final value of the RU dc voltage is shown as a function of amplitude and phase noise of the GU, as well as additive noise at the RU.

[44]$\mathbf{k}$ can be evaluated using a localized EM simulation or a simplified coupling model.

[45]This method is known to work for equal amplitude driven elements, but it is hypothesized that this relationship holds for the non-constant drive as well. No counterexample has been found yet.
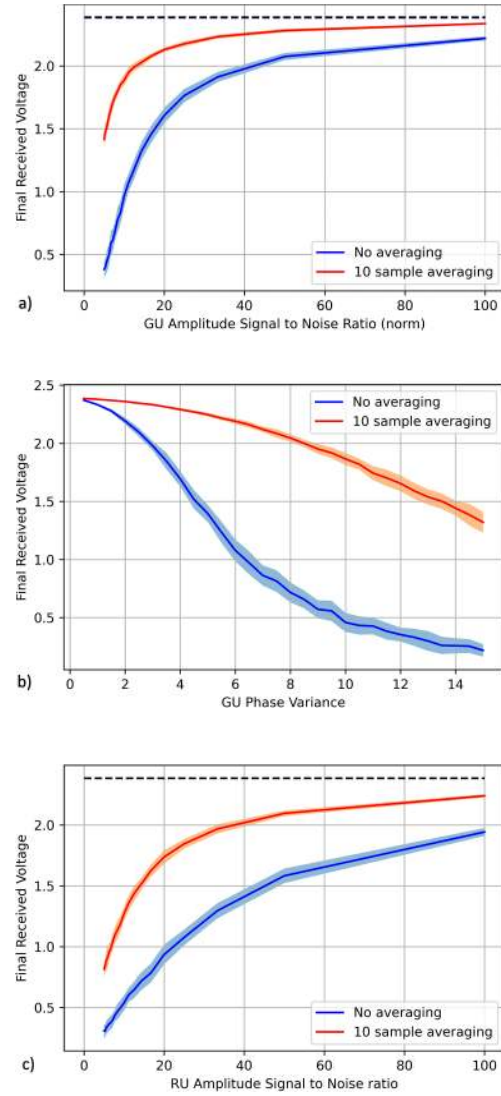

Fig. 29. Effect of (a) GU-amplitude-noise-induced SNR alone, (b) GU random phase noise variance alone, and (c) RU amplitude-noise-induced SNR on the final RU dc voltage alone. 1-σ error band for 50 runs. The dashed asymptotes show the noiseless final value.

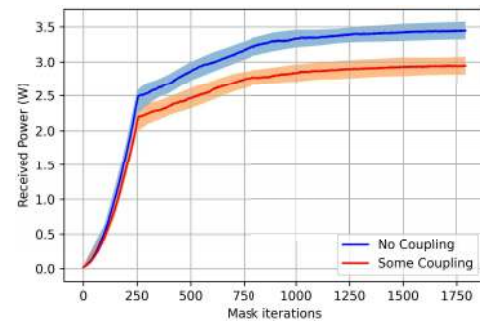

Fig. 30. Effect of coupling on the optimized voltage of a 16×16 GU ($\text{SNR}_{\text{amp}} = 20$ dB), averaged over 50 runs. Single-element sweeps were used throughout the optimization, and 4% of the power to an element couples to other elements.

Fig. 30 shows the effect of element coupling among the GU elements on the performance of the algorithm versus the performance without the element coupling. The presence of the coupling matrix causes some of the power from one port
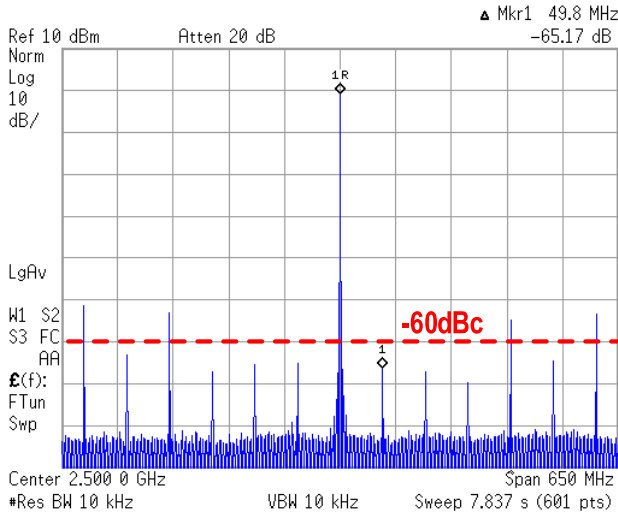
(a)
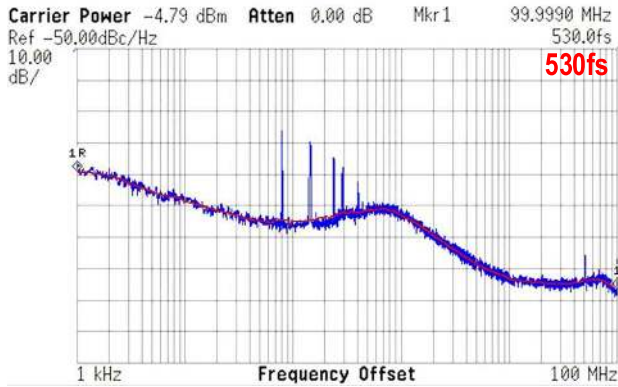
(b)

Fig. 31. (a) Output spectrum of the central 2.5-GHz PLL. (b) Phase noise spectrum of a single 10-GHz output.
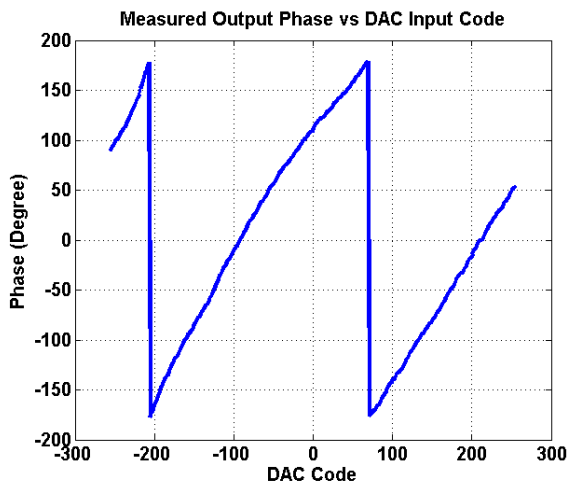

Fig. 32. CMU output phase versus the digital input code to the current DAC.

to be scattered or absorbed by other ports. Element coupling lowers the achievable power by the basic algorithm. This is why even though the noise levels in Fig. 30 are the same, the received power is less.
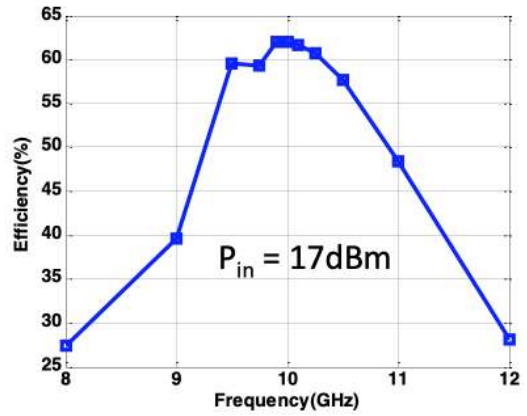

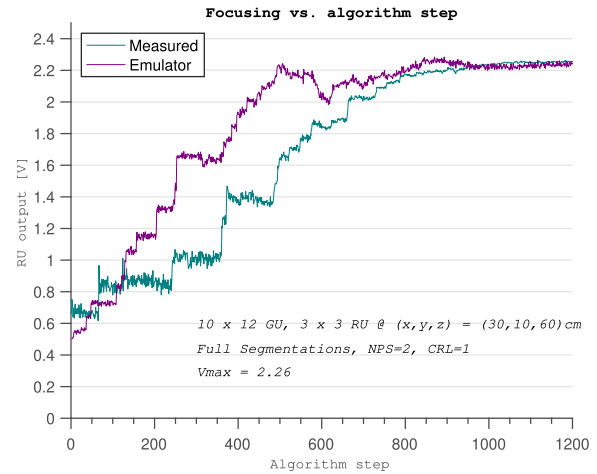Fig. 33. Measured efficiency of the RU rectifier versus frequency.

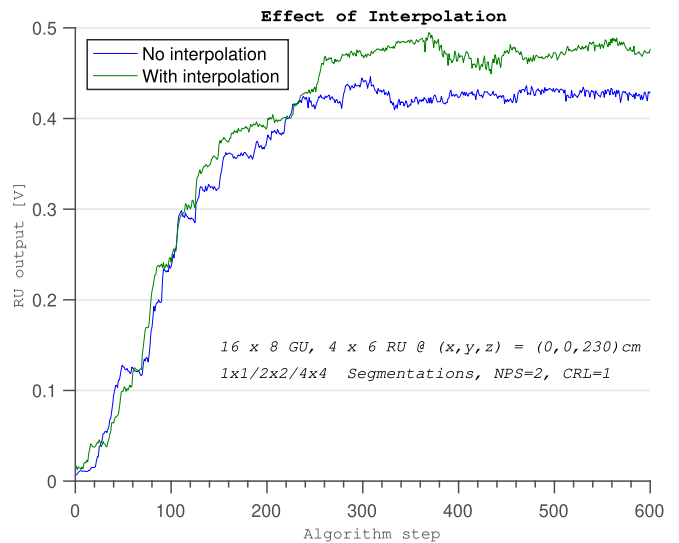Fig. 34. Sample measured and emulator generated dc voltage at the RU with a 10×12 GU.

Fig. 35. Measured effectiveness of interpolation.

VIII. MEASUREMENT RESULTS

The output spectrum of the central PLL and the phase noise profile of a single output channel are shown in Fig. 31. The low reference spurs within the antenna bandwidth and
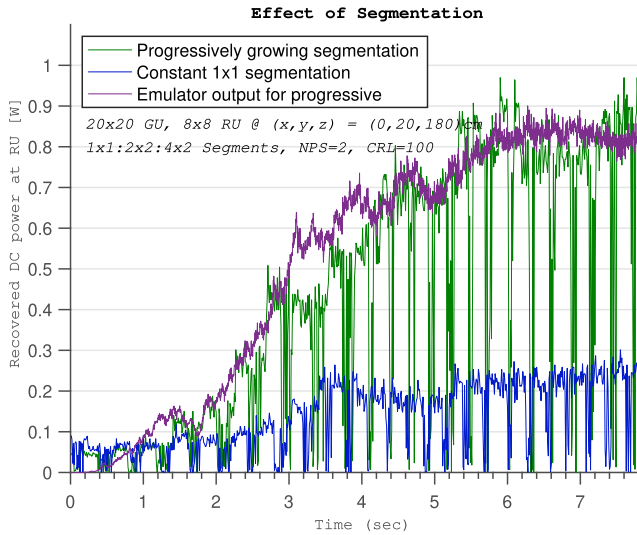
Fig. 36. Measured effect of increasing mask size on the final focused power of a 400-element GU.
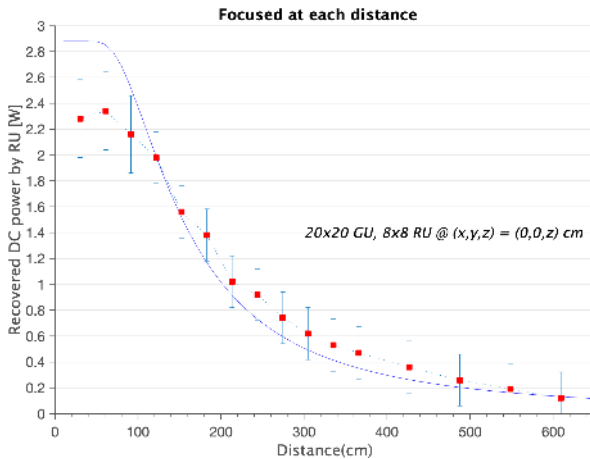

Fig. 37. Measured power versus distance after focusing at each distance versus the estimate obtained using (11). The focusing algorithm uses an NPS $= 2$ and a CRL $= 100$, as well as a $1 \times 1{:}2 \times 2{:}2 \times 4{:}4 \times 4$ segmentation progression.
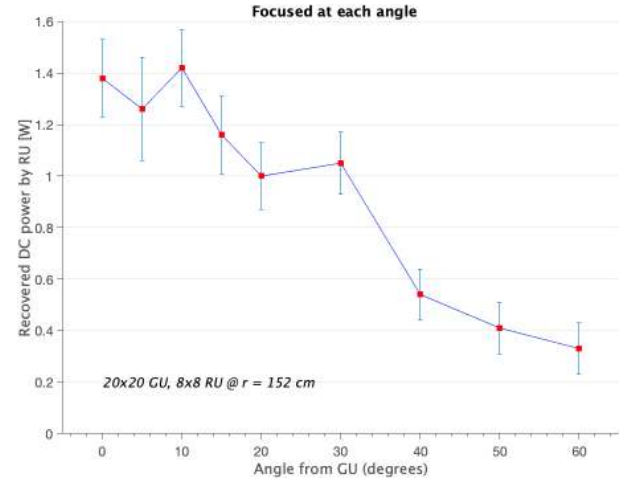

Fig. 38. Measured power versus angle from GU central normal axis after focusing at each angle at a distance of 152 cm. The focusing algorithms was called with an NPS $= 2$, CRL $= 100$, and a $1 \times 1{:}2 \times 2{:}2 \times 4{:}4 \times 4$ segmentation progression.
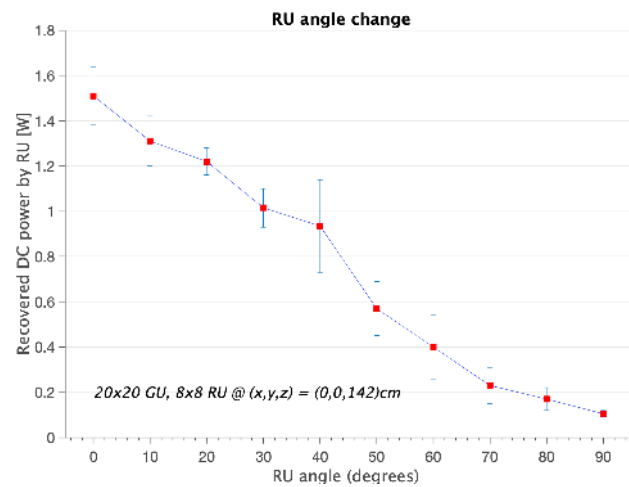

Fig. 39. Measured power versus angle of the RU from the line connecting the center of the RU to the center of the GU at a distance of 142 cm. The focusing algorithms was called with an NPS $= 2$, CRL $= 100$, and a $1 \times 1{:}2 \times 2{:}2 \times 4{:}4 \times 4$ segmentation progression.

the measured integrated rms phase noise are important for focusing algorithms that maximize the signal power at the carrier frequency. The measured output phase versus the digital control word is shown in Fig. 32. The measurement results confirm a monotonic phase shift versus the input code as expected from a thermometer-coded current DAC. The observed non-linearity is the result of non-linearity in the phase detector of the CMU.

The overall measured efficiency of the RU rectifier is shown as a function of the frequency of operation in Fig. 33, where the RU rectification maximum efficiency of 63% is designed to be centered at 10 GHz at $+17$-dBm input power in this particular implementation.

Fig. 34 shows a sample of the progression of the measured dc voltage at the RU as the focusing algorithm runs with 10×12 GU and a 3×3 RU. In this case, the algorithm runs with the full 10×12 mask size for all iterations. A companion sample result from the emulator of Section VII is shown on the same plots. The observed large jumps after periods of relative

quiet are characteristic of larger mask size, visible in both the measurement and emulator results.

Fig. 35 compares focusing where the best phase setting is interpolated using sines and cosines versus simply choosing the phase setting with the highest power, as explained in Section IV-D. The interpolation can improve the convergence of the focusing and the delivered higher final power in certain settings. It should be noted that the received power at RU is proportional to the voltage squared.

Fig. 36 shows the recovered dc power of a 20×20 GU at a distance of approximately 2 m in two different scenarios, one where the segmentation (mask size) is kept at 1×1 throughout all iterations versus the segmentation increasing progressively as the PSR decreases. It clearly demonstrates the benefits of increasingly large segmentation (mask) size in large arrays to improve the SNR, as is evident from the higher final focused power. It also demonstrates the ability to batch process by running with longer CRLs (in this case, 100) in systems with
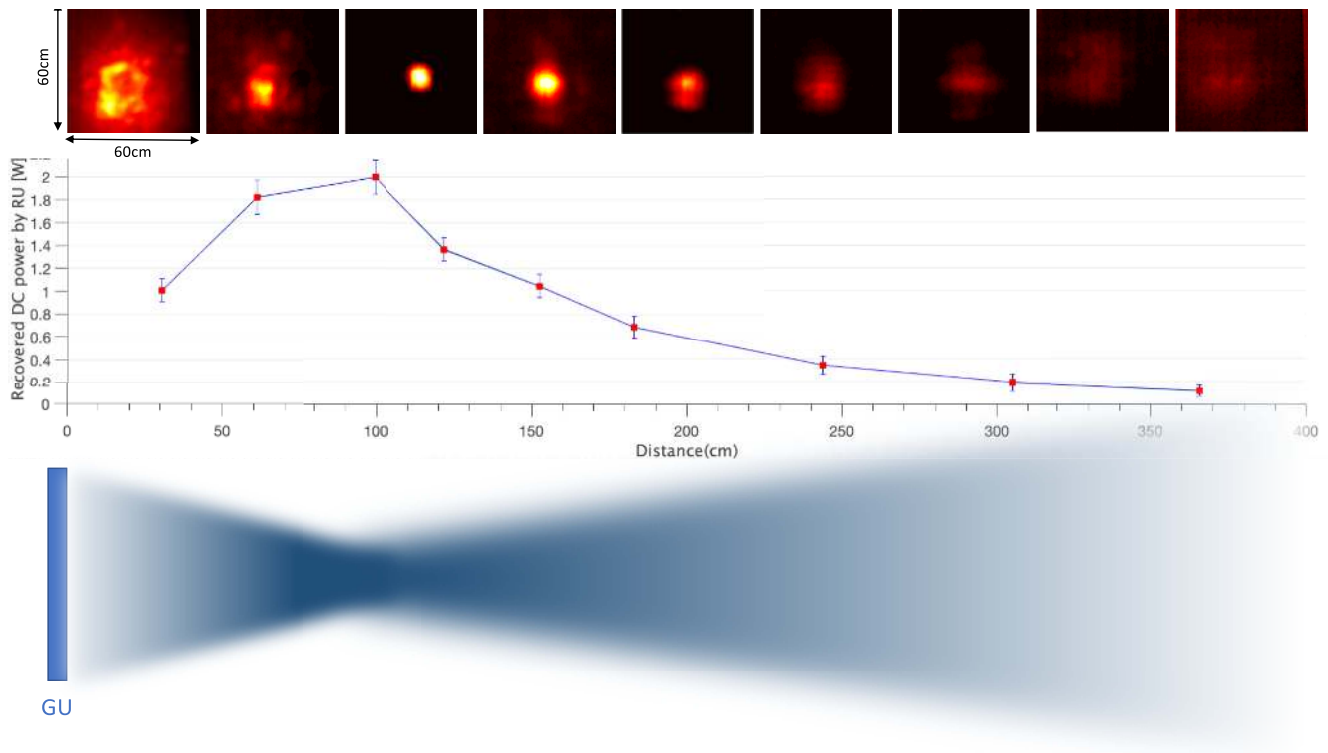
Fig. 40. Field strength slices at various distances from the 400-element GU of Fig. 22(c), for a beam focused using the algorithm of Section IV at a 1-m distance from the GU along its centerline. The thermal images of the slide corresponding to the distances associated with the measurement recovered dc data points in red on the plot. The focusing behavior visualized by the lower conceptual field profile is clearly seen from the thermal images on the top.

low bandwidth and/or large latency communication link. This performance difference between the standard approach and the proposed algorithm is generally observed in this system and is not limited to this particular example.

A suite of additional measurements is performed on the 20×20 (400-element) GU. In one set of measurements, the RU is placed at different distances from the GU, the focusing algorithm is run multiple times, and the dc output power of the RU into the optimum resistive load is recorded. Fig. 37 shows a plot of the recovered dc power when the GU is focused independently for each different location versus distance from the GU. The solid line shows the approximate estimate provided by (11), taking into account the estimated element radiated power and the RU's radiative and rectification performance estimates.

The system and its operation were evaluated under various geometric arrangements of the GU and RU, some of which will be discussed next. The performance of the system when the RU is placed at various angles off the center axis of the GU is evaluated by maintaining a constant distance between the GU and RU while changing the angle of the GU, as shown in Fig. 38. This can, for example, correspond to a GU mounted on the ceiling and powering the RUs in different locations in the room (e.g., on tabletops). For every new angle, the focusing algorithm is run again, and the dc power delivered to the optimum resistive load is recorded. The measured powers correspond to a 3-dB FOV of more than 70° in either direction.[46]

---

[46]This for a 2.75-m (9-ft) ceiling that roughly corresponds to a circle with a radius of 1.4 m (4.5ft) or an approximate "3-dB area" of 6 m^2 (60 ft^2).

The effect of RU varying orientation is evaluated in Fig. 39, where the RU angle with respect to the line connecting its center to the center of GU is varied between 0 and 90° and the average of the measured values is plotted. As expected, the power drops as a smaller apparent angle of the RU is exposed to the GU, but there is graceful degradation. As explained in Section VI-C, the RU is capable of collecting power from a broad range of angles due to the power aggregation at dc, where phase alignment is guaranteed. This is, of course, subject to a reduction in the apparent aperture of $\cos(\theta)$ in an infinite array due to energy considerations. It is noteworthy that, due to the finite dimensions of the RU array, it is still capable of collecting some power (due to endfire element patterns and edge effects, as evident from Fig. 39).

Finally, two sets of direct measurements capture and visualize the RF lensing and focusing operation. In the first set shown in Fig. 40, the algorithm in Section IV is used to focus the power on an 8×8-RU at approximately 1 m away from the GU. The RU is subsequently removed, and a 60 cm × 60 cm RF absorber foam in thermal equilibrium with the ambient is placed parallel to the GU front plane and is exposed to the RF beam for 90 s. A thermal camera is used to image it immediately at the end of the 90-s period, in essence creating a slice of the field power density at each distance. These slices clearly show the initial convergence and the subsequent divergence of the field under focusing operation of RF lensing. In a second experiment, as depicted in Fig. 41, the RU is placed back at the 1-m focal point and is loaded by the optimum dc load to draw the maximum power, and the field distribution is measured again. The field behind the RU is
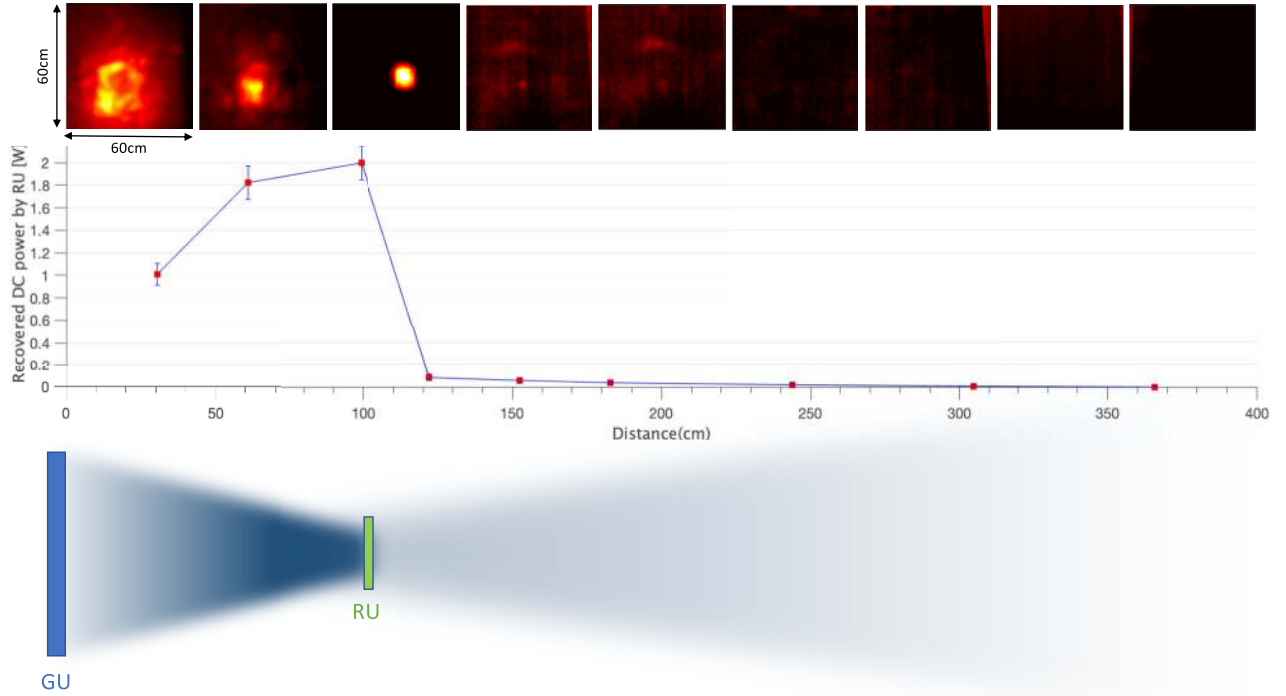
Fig. 41. Field strength slices at various distances from the 400-element GU, under the same setting of Fig. 40, in the presence of an 8×8 RU at the focal point, feeding power into a resistive load. The thermal image slices clearly demonstrate how under normal operation the energy is mostly absorbed by the RU and the spillover is minimized behind the RU, as also visualized by the conceptual field profile on the bottom.

clearly diminished, showing that most of the RF power is absorbed by the RU and very little spillover is seen.[47]

IX. CONCLUSION

An overview of focusing and refocusing in large arrays with an emphasis on WPT-AD was given through the study of the EM behavior, system architecture, circuit design, and algorithms leading to an approach based on adaptive, dynamic, and multi-dimensional spatially independent basis masks. The proposed approach is compatible with both near-field focusing and far-field operation and can focus the energy onto small focal points in the near- and far-field. Several examples of system operation with different settings, distances, and geometries are shown in a 400-element GU build using custom-designed CMOS ICs. The GU works collaboratively with the RU to maximize the amount of wireless power transferred with the result that more than 2 W of dc power can be recovered at distances greater than 1 m, and power can be projected more than 10 m. This works serves as another step toward the full realization of WPT-AD.

APPENDIX
CONSTRUCTION OF 2-D ORTHOGONAL BASES AND PSEUDO-HADAMARD MATRICES

The Hadamard matrices, originally invented by Sylvester [36], are square matrices whose elements are either $+1$ or -1

and whose rows (and columns) are pairwise orthogonal to each other. Namely

$$H_n H_n^T = n I_n \qquad (40)$$

where H_n is the $n \times n$ Hadamard matrix, H_n^T is its transpose, and I_n is the $n \times n$ identity matrix.

Originally, Sylvester's method allowed the construction of the Hadamard matrices for which the number of rows (and columns) is 2^k, where k is an integer. This is accomplished by using a Kronecker product (replacing each element with the other matrix multiplied by the element) from the 2×2-Hadamard matrix H_2

$$H_2 = \begin{bmatrix} 1 & 1 \\ 1 & -1 \end{bmatrix} \qquad (41)$$

namely

$$H_{2^k} = \begin{bmatrix} H_{2^{k-1}} & H_{2^{k-1}} \\ H_{2^{k-1}} & -H_{2^{k-1}} \end{bmatrix} = H_2 \otimes H_{2^{k-1}} \qquad (42)$$

where $\otimes$ represents the Kronecker product.[48] For example

$$H_4 = \begin{bmatrix} H_2 & H_2 \\ H_2 & -H_2 \end{bmatrix} \overset{\text{reorder}}{=} \begin{bmatrix} 1 & 1 & 1 & 1 \\ 1 & 1 & -1 & -1 \\ 1 & -1 & -1 & 1 \\ 1 & -1 & 1 & -1 \end{bmatrix}. \qquad (43)$$

In the reordering step, the rows are rearranged such that the row with the least number of value changes from element to element becomes the top row. The next row has the second-to-least number of changes element-to-element, and so

---

[47]This is important both from the overall recovery rate and meeting the regulatory requirements for EM exposures and interference.

[48]The Kronecker product is obtained by replacing each element of the first matrix with the second matrix multiplied by the value of the element of the first matrix in question.

on, with the bottom row having the largest number of element-to-element changes. Sylvester's construction only generates matrices with powers of 2. The Hadamard conjecture [37] states that the Hadamard matrices exist for sizes that are integer multiples of 4 (H_{4k}). They can be constructed either analytically or by computers.

In general, a perfectly orthogonal basis mask set of size $M \times N$ can be generated if H_M and H_N (Hadamard matrices of sizes $M \times M$ and $N \times N$) exist. Rows (or columns) of $N \times N$-Hadamard matrices provide N 1-D vectors of length N. Thus, individual $M \times N$-masks can be generated by multiplying a column of the H_M matrix by a row of the H_N matrix to generate an $M \times N$ matrix (a mask). A different mask is generated for each of the MN permutations, as shown in Fig. 11.

However, if one of the dimensions of the full array (M or N) or any of the dimensions of the desired segmentation (M_s or N_s) is not a multiple of 4, or if one of the requisite Hadamard matrices does not exist, then perfectly orthogonal masks cannot be generated.

Here, we propose a construct that we call a pseudo-Hadamard matrix for matrix sizes that are not multiples of 4 (including odd numbers). Since it not possible to get $\hat{H}\hat{H}^T$ to be exactly n times the identity matrix, I_n, it should instead be as close to it as possible. This means that the off-diagonal elements should be as close to zero as possible. Various measures of this "closeness" can be considered, such as the sum of the squares of the off-diagonal elements, the sum of their absolute values, the maximum absolute value among off-diagonal elements, or simply the value of the largest deviant from 0. For example, the objective of minimizing the squares of the off-diagonal elements can be expressed as

$$\min \langle \hat{H}_n \hat{H}_n^T - n I_n, \hat{H}_n \hat{H}_n^T - n I_n \rangle. \qquad (44)$$

These metrics can be applied either analytically or computationally to generate the pseudo-Hadamard matrices. Examples of such are shown in Fig. 42 for square matrix sizes of 3, 5, 7, and 10. The pseudo-Hadamard matrices can be used to generate pseudo-orthogonal 2-D masks for the algorithm discussed in Section IV, which forms a pseudo-orthogonal basis. The basis is close to orthogonal if the inner product of $M \times N$-masks $\hat{M}_i$ and $\hat{M}_j$ is as close to MN when $i = j$ and as close to the zero matrix for $i \neq j$, or in short

$$\min |\langle \hat{M}_i, \hat{M}_j \rangle - MN \delta_{ij}| \qquad (45)$$
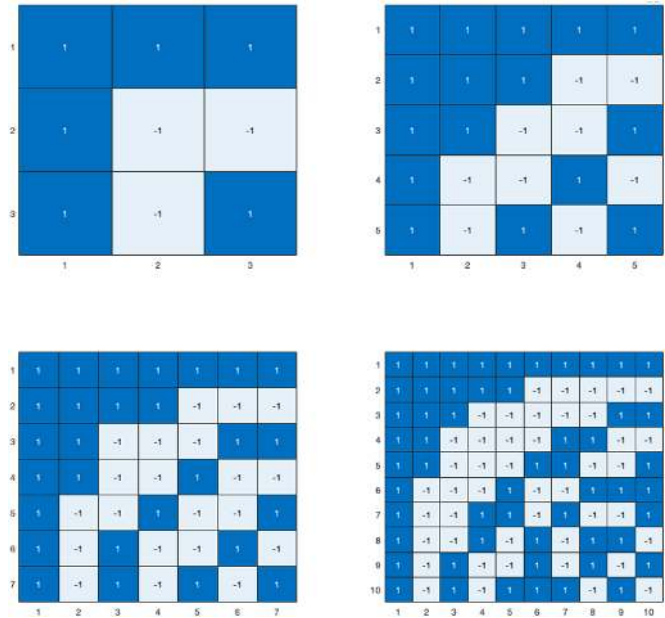
where δ_{ij} is the Kronecker delta.

ACKNOWLEDGMENT AND CONTRIBUTIONS

Fig. 42. Example pseudo-Hadamard matrices of sizes 3, 5, 7, and 10, where an actual Hadamard matrix does not exist.

REFERENCES

[1] K. F. Braun. (Dec. 11, 1909). *Electrical Oscillators and Wireless Telegraphy, Nobel Lecture*. [Online]. Available: https://www.nobelprize.org/prizes/physics/1909/braun/lecture/

[2] N. Amitay, *Theory and Analysis of Phased Array Antennas*. New York, NY, USA: Wiley, 1972.

[3] A. J. Fenn, *Adapt. Antennas Phased Arrays for Radar Communications*. Norwood, MA, USA: Artech House, 2008.

[4] J. D. Kraus and R. J. Marhefka, *Antennas for all Applications*. 3rd ed. New York, NY, USA: McGraw-Hill, 2002.

[5] R. J. Mailloux, *Phased Array Antenna Handbook*. 2nd ed. Norwood, MA, USA: Artech House, 2005.

[6] W.-D. Wirth, *Radar Techniques Using Array Antennas*. 2nd ed. Edison, NJ, USA: IET, 2005.

[7] K. Sengupta and A. Hajimiri, "Smart RF lensing: Efficient, dynamic and mobile wireless power transfer," U.S. Patent 10 367 380, Nov. 9, 2012.

[8] J. Herd, "Experimental results from a self-calibrating digital beamforming array," in *Proc. Int. Symp. Antennas Propag. Soc., Merging Technol.*, vol. 1, 1990, pp. 384–387.

[9] K.-M. Lee, R.-S. Chu, and S.-C. Liu, "A built-in performance-monitoring/fault isolation and correction (PM/FIC) system for active phased-array antennas," *IEEE Trans. Antennas Propag.*, vol. 41, no. 11, pp. 1530–1540, Nov. 1993.

[10] R. Ishii, K. Shiramatsu, T. Haruyama, N. Orime, and T. Katagi, "A built-in correction method of the phase distribution of a phased array antenna," in *Antennas Propag. Soc. Symp. Dig.*, vol. 2, Jun. 1991, pp. 1144–1147.

[11] A. Safaripour, B. Asghari, and A. Hajimiri, "Proximal-field radiation sensors for millimeter-wave integrated radiators," in *Proc. IEEE Radio Freq. Integr. Circuits Symp. (RFIC)*, Jun. 2018, pp. 256–259.

[12] H. M. Aumann, A. J. Fenn, and F. G. Willwerth, "Phased array antenna calibration and pattern prediction using mutual coupling measurements," *IEEE Trans. Antennas Propag.*, vol. 37, no. 7, pp. 844–850, Jul. 1989.

[13] W. T. Patton and L. H. Yorinks, "Near-field alignment of phased-array antennas," *IEEE Trans. Antennas Propag.*, vol. 47, no. 3, pp. 584–591, Mar. 1999.

[14] C. Fulton, M. Yeary, D. Thompson, J. Lake, and A. Mitchell, "Digital phased arrays: Challenges and opportunities," *Proc. IEEE*, vol. 104, no. 3, pp. 487–503, Mar. 2016.

[15] A. C. Fikes, A. Safaripour, F. Bohn, B. Abiri, and A. Hajimiri, "Flexible, conformal phased arrays with dynamic array shape self-calibration," in *IEEE MTT-S Int. Microw. Symp. Dig.*, Jun. 2019, pp. 1458–1461.

[16] M. R. M. Hashemi *et al.*, "A flexible phased array system with low areal mass density," *Nature Electron.*, vol. 2, no. 5, pp. 195–205, May 2019, doi: 10.1038/s41928-019-0247-9.

[17] M. Gal-Katziri, A. Fikes, F. Bohn, B. Abiri, M. R. Hashemi, and A. Hajimiri, "Scalable, deployable, flexible phased array sheets," in *IEEE MTT-S Int. Microw. Symp. Dig.*, Aug. 2020, pp. 1085–1088.

[18] H. Wilden and J. Ender, "The crow's nest antenna-experimental results," in *Proc. Int. Conf. Radar*, May 1990, pp. 280–285.

[19] R. Fatemi, A. Khachaturian, and A. Hajimiri, "A nonuniform sparse 2-D large-FOV optical phased array with a low-power PWM drive," *IEEE J. Solid-State Circuits*, vol. 54, no. 5, pp. 1200–1215, May 2019.

[20] A. Darbinian, A. Hajimiri, A. Khachatourian, and S. M. Fatemi, "Photonics adaptive beam forming with a polar lattice," U.S. Patent 62 562 925, Sep. 25, 2017.

[21] D. E. Williams, C. Dorn, S. Pellegrino, and A. Hajimiri, "Origami-inspired shape-changing phased array," in *Proc. 50th Eur. Microw. Conf. (EuMC)*, Utrecht, The Netherlands, 2020.

[22] I. Asimov, "Reason," Astounding Science Fiction, Apr. 1941.

[23] W. C. Brown, "The history of power transmission by radio waves," *IEEE Trans. Microw. Theory Techn.*, vol. MTT-32, no. 9, pp. 1230–1242, Sep. 1984.

[24] X. Guan and A. Hajimiri, "A 24-GHz CMOS front-end," *IEEE J. Solid-State Circuits*, vol. 39, no. 2, pp. 368–373, Feb. 2004.

[25] X. Guan, H. Hashemi, and A. Hajimiri, "A fully integrated 24-GHz eight-element phased-array receiver in silicon," *IEEE J. Solid-State Circuits*, vol. 39, no. 12, pp. 2311–2320, Dec. 2004.

[26] A. Hajimiri, A. Komijani, A. Natarajan, R. Chunara, X. Guan, and H. Hashemi, "Phased array systems in silicon," *IEEE Commun. Mag.*, vol. 42, no. 8, pp. 122–130, Aug. 2004.

[27] A. Natarajan, A. Komijani, and A. Hajimiri, "A fully integrated 24-GHz phased-array transmitter in CMOS," *IEEE J. Solid-State Circuits*, vol. 40, no. 12, pp. 2502–2514, Dec. 2005.

[28] A. Hajimiri, H. Hashemi, A. Natarajan, X. Guan, and A. Komijani, "Integrated phased array systems in silicon," *Proc. IEEE*, vol. 93, no. 9, pp. 1637–1655, Sep. 2005.

[29] A. Natarajan, A. Komijani, X. Guan, A. Babakhani, and A. Hajimiri, "A 77-GHz phased-array transceiver with on-chip antennas in silicon: Transmitter and local LO-path phase shifting," *IEEE J. Solid-State Circuits*, vol. 41, no. 12, pp. 2807–2819, Dec. 2006.

[30] A. Babakhani, X. Guan, A. Komijani, A. Natarajan, and A. Hajimiri, "A 77-GHz phased-array transceiver with on-chip antennas in silicon: Receiver and antennas," *IEEE J. Solid-State Circuits*, vol. 41, no. 12, pp. 2795–2806, Dec. 2006.

[31] C. Marcu *et al.*, "A 90 nm CMOS low-power 60 GHz transceiver with integrated baseband circuitry," *IEEE J. Solid-State Circuits*, vol. 44, no. 12, pp. 3434–3447, Dec. 2009.

[32] V. Jain, F. Tzeng, L. Zhou, and P. Heydari, "A single-chip dual-band 22–29-GHz/77–81-GHz BiCMOS transceiver for automotive radars," *IEEE J. Solid-State Circuits*, vol. 44, no. 12, pp. 3469–3485, Dec. 2009.

[33] M. Nariman, F. Shirinfar, A. P. Toda, S. Pamarti, A. Rofougaran, and F. De Flaviis, "A compact 60-GHz wireless power transfer system," *IEEE Trans. Microw. Theory Techn.*, vol. 64, no. 8, pp. 2664–2677, Aug. 2016.

[34] H. B. Curry, "The method of steepest descent for non-linear minimization problems," *Quart. Appl. Math.*, vol. 2, no. 3, pp. 258–261, 1944.

[35] S. Boyd and L. Vandenberghe, *Convex Optimization*. Cambridge, U.K.: Cambridge Univ., The Edinburgh Building, 2004.

[36] J. J. Sylvester, "LX. Thoughts on inverse orthogonal matrices, simultaneous signsuccessions, and tessellated pavements in two or more colours, with applications to Newton's rule, ornamental tile-work, and the theory of numbers," *London, Edinburgh, Dublin Phil. Mag. J. Sci.*, vol. 34, no. 232, pp. 461–475, Dec. 1867.

[37] A. Hedayat and W. D. Wallis, "Hadamard matrices and their applications," *Ann. Statist.*, vol. 6, no. 6, pp. 1184–1238, Nov. 1978, doi: 10.1214/aos/1176344370.

[38] F. Bohn, B. Abiri, and A. Hajimiri, "Fully integrated CMOS X-band power amplifier quad with current reuse and dynamic digital feedback (DDF) capabilities," in *Proc. IEEE Radio Freq. Integr. Circuits Symp. (RFIC)*, Jun. 2017, pp. 208–211.

[39] M. Gal-Katziri and A. Hajimiri, "A sub-picosecond hybrid DLL for large-scale phased array synchronization," in *Proc. IEEE Asian Solid-State Circuits Conf. (A-SSCC)*, Nov. 2018, pp. 231–234.

[40] H. Wang and A. Hajimiri, "A wideband CMOS linear digital phase rotator," in *Proc. IEEE CICC*, Sep. 2007, pp. 671–674.

[41] S. Jeon *et al.*, "A scalable 6-to-18 GHz concurrent dual-band quad-beam phased-array receiver in CMOS," *IEEE J. Solid-State Circuits*, vol. 43, no. 12, pp. 2660–2673, Dec. 2008.

[42] R. Fatemi, P. P. Khial, A. Khachaturian, and A. Hajimiri, "Breaking FOV-aperture trade-off with multi-mode nano-photonic antennas," *IEEE J. Sel. Topics Quantum Electron.*, vol. 27, no. 1, pp. 1–14, Jan. 2021.

[43] T. Reveyrand, I. Ramos, and Z. Popović, "Time-reversal duality of high-efficiency RF power amplifiers," *Electron. Lett.*, vol. 48, no. 25, pp. 1607–1608, Dec. 2012.

[44] T. Reveyrand, I. Ramos, and Z. Popović, "Time-reversal duality of high-efficiency RF power amplifiers," *Electron. Lett.*, vol. 48, no. 25, pp. 4043–4052, Nov. 2012.

Ali Hajimiri (Fellow, IEEE) received the B.S. degree in electronics engineering from the Sharif University of Technology, Tehran, Iran, in 1994, and the M.S. and Ph.D. degrees in electrical engineering from Stanford University, Stanford, CA, USA, in 1996 and 1998, respectively.

He has been with Philips Semiconductors, where he worked on a BiCMOS chipset for GSM and cellular units from 1993 to 1994. In 1995, he was with Sun Microsystems, Sunnyvale, CA, where he worked on the UltraSPARC microprocessors cache RAM design methodology. During summer 1997, he was with Lucent Technologies (Bell Labs), Murray Hill, NJ, USA, where he investigated low-phase-noise integrated oscillators. In 1998, he joined the Faculty of the California Institute of Technology, Pasadena, CA, where he is currently the Bren Professor of Electrical Engineering and Medical Engineering, the Director of the Microelectronics Laboratory, and a Co-Director of Space Solar Power Project. In 2002, he co-founded Axiom Microdevices Inc., Irvine, CA, whose fully integrated CMOS phased array (PA) has shipped around 400 000 000 units and was acquired by Skyworks Inc., Irvine, in 2009. He is also a Co-Founder of GuRu Wireless Inc., Pasadena. He is the author of *Analog: Inexact Science, Vibrant Art* (Early Draft, 2020), a book on fundamental principles of analog circuit design, and *The Design of Low Noise Oscillators* (Boston, MA, USA: Springer). He has authored or coauthored more than 250 refereed journal and conference technical articles and has been granted more than 120 U.S. patents with many more pending applications. His research interests are high-speed and high-frequency integrated circuits for applications in sensors, photonics, biomedical devices, and communication systems.

Prof. Hajimiri is a fellow of the National Academy of Inventors (NAI). He was selected for the TR35 top innovator's list. He was a recipient of the Microwave Prize. He won the Feynman Prize for Excellence in Teaching, Caltech's most prestigious teaching honor, the Caltech's Graduate Students Council Teaching and Mentoring Award, and the Associated Students of Caltech Undergraduate Excellence in Teaching Award. He was the Gold Medal Winner of the National Physics Competition and the Bronze Medal Winner of the 21st International Physics Olympiad, Groningen, The Netherlands. He was recognized as one of the top-ten contributors to ISSCC. He was a co-recipient of the IEEE Journal of Solid-State Circuits Best Paper Award, the International Solid-State Circuits Conference (ISSCC) Jack Kilby Outstanding Paper Award, the RFIC Best Paper Award, and the IMS Best Advance Practices Awards, a two-time co-recipient of the CICC Best Paper Award, and the three-time winner of the IBM Faculty Partnership Award, the National Science Foundation CAREER Award, and the Okawa Foundation Award. He has served as a Distinguished Lecturer of the IEEE Solid-State and Microwave Societies. He has served on the Technical Program Committee of the International Solid-State Circuits Conference (ISSCC), as an Associate Editor of the IEEE JOURNAL OF SOLID-STATE CIRCUITS (JSSC) and the IEEE TRANSACTIONS ON CIRCUITS AND SYSTEMS II (TCAS), a member of the Technical Program Committees of the International Conference on Computer Aided Design (ICCAD), a Guest Editor of the IEEE TRANSACTIONS ON MICROWAVE THEORY AND TECHNIQUES, and a Guest Editorial Board Member of the TRANSACTIONS OF INSTITUTE OF ELECTRONICS, INFORMATION AND COMMUNICATION ENGINEERS OF JAPAN (IEICE).

Behrooz Abiri (Member, IEEE) received the Ph.D. degree from the California Institute of Technology (Caltech), Pasadena, CA, USA, in 2017.

He co-founded GuRu Wireless Inc., Pasadena, in 2017, to bring true wireless power technology into the market, where he is currently serving as the Chief Technology Officer and leading the Engineering Team. He holds 25 granted U.S. patents. His research interests include RF and millimeter-wave transceivers, monolithic mm-wave power amplifiers and rectifiers, optical and mm-wave phased arrays, and their applications in wireless power transmission systems.

Dr. Abiri has been awarded the Charles Wilts Prize for best Ph.D. thesis from the Electrical Engineering Department, Caltech, in 2017, the IEEE Solid State Circuits Society Predoctoral Achievement Award in 2014, the Analog Devices Outstanding Student Designer Award in 2013, the Caltech Ph.D. Fellowship in 2011, and the Edward S. Rogers Scholarship from the Electrical Engineering and Computer Science (EECS) Department, University of Toronto, in 2009. He is also the Gold Medal Winner of the 16th National Physics Olympiad, Iran, in 2003, and the 35th International Physics Olympiad, Pohang, South Korea, in 2004.

Florian Bohn (Member, IEEE) received the M.S. degree in electrical and computer engineering from the University of California at Santa Barbara, Santa Barbara, CA, USA, in 2003, and the B.S. (Hons.) and Ph.D. degrees in electrical engineering from the California Institute of Technology (Caltech), Pasadena, CA, USA, in 2001 and 2012, respectively.

From 2003 to 2005, he was an RF IC Design Engineer with Axiom Microdevices Inc., Irvine, CA, USA (now Skyworks Solutions, Inc.), where he worked on the design and testing of active and passive circuits for the world's first GSM/GPRS CMOS power amplifiers with total shipments exceeding 400M units. From 2011 to 2013, he developed and designed solid-state PLL and CDR circuits for novel test and measurement solutions at Agilent Laboratories (now Keysight Laboratories), Santa Clara, CA. From 2013 to 2017, he developed innovative systems and circuits for RF-based wireless power transfer systems, most recently as a Lead Scientific Researcher at Caltech. Among other activities, he was managing engineering and operational activities of the microwave system implementation of Caltech's Space-Based Solar Power Project (SSPP). In 2017, he co-founded GuRu Wireless, Inc. (formerly known as Auspion, Inc.), Pasadena, which is marketing wireless power solutions for consumer and industrial applications. Having served as GuRu's Vice President of Engineering, he is the company's Chief Executive Officer and a member of the Board of Directors. He has research and commercial interests in broad areas of high-frequency electronic systems and circuits, with an emphasis on solid-state solutions.

Dr. Bohn received the Conexant Scholarship and the Analog Devices Outstanding Student Designer Award.

Matan Gal-Katziri (Member, IEEE) received the B.S. degree in physics and electrical engineering from Ben-Gurion University, Beersheba, Israel, in 2009, and the M.S. and Ph.D. degrees in electrical engineering from the California Institute of Technology (Caltech), Pasadena, CA, USA, in 2016 and 2020, respectively.

He is currently a Post-Doctoral Research Associate with the Department of Electrical Engineering, Caltech. He is a part of Caltech's Solar-Space Power Project (SSPP) RF team. His research interests are integrated and large-scale phased arrays and precision sensors.

Dr. Gal-Katziri was awarded the Analog Devices Outstanding Student Designer Award in 2015.

Mohith H. Manohara (Student Member, IEEE) is currently pursuing the B.S. degree in electrical engineering with the California Institute of Technology (Caltech), Pasadena, CA, USA.

He joined the Caltech High Speed Integrated Circuits (CHIC) Group in 2018 as an Undergraduate Researcher. His current research interests include RF systems for wireless sensing, communication, and robotics applications.

Dr. Manohara received the Henry Ford II Scholar Award for high academic standing in 2020.